Space Sci Rev (2020) 216:128
https://doi.org/10.1007/s11214-020-00740-4

Radar Imager for Mars' Subsurface Experiment—RIMFAX

Svein-Erik Hamran[1] · David A. Paige[2] · Hans E.F. Amundsen[3] · Tor Berger[4] · Sverre Brovoll[4] · Lynn Carter[5] · Leif Damsgård[4] · Henning Dypvik[1] · Jo Eide[6] · Sigurd Eide[1] · Rebecca Ghent[7] · Øystein Helleren[4] · Jack Kohler[8] · Mike Mellon[9] · Daniel C. Nunes[10] · Dirk Plettemeier[11] · Kathryn Rowe[2] · Patrick Russell[2] · Mats Jørgen Øyan[4]

Received: 15 May 2020 / Accepted: 25 September 2020 / Published online: 3 November 2020

Abstract The Radar Imager for Mars' Subsurface Experiment (RIMFAX) is a Ground Penetrating Radar on the Mars 2020 mission's *Perseverance* rover, which is planned to land near a deltaic landform in Jezero crater. RIMFAX will add a new dimension to rover investigations of Mars by providing the capability to image the shallow subsurface beneath the rover. The principal goals of the RIMFAX investigation are to image subsurface structure, and to provide information regarding subsurface composition. Data provided by RIMFAX will aid Perseverance's mission to explore the ancient habitability of its field area and to select a set of promising geologic samples for analysis, caching, and eventual return to Earth. RIMFAX is a Frequency Modulated Continuous Wave (FMCW) radar, which transmits a signal swept through a range of frequencies, rather than a single wide-band pulse. The operating frequency range of 150–1200 MHz covers the typical frequencies of GPR used in geology. In general, the full bandwidth (with effective center frequency of 675 MHz) will be used for

The Mars 2020 Mission
Edited by Kenneth A. Farley, Kenneth H. Williford and Kathryn M. Stack

✉ S.-E. Hamran
s.e.hamran@its.uio.no

1 University of Oslo, Oslo, Norway

2 University of California, Los Angeles, CA, USA

3 Vestfonna Geophysical, Trondheim, Norway

4 Forsvarets Forskningsinstitutt, Kjeller, Norway

5 University of Arizona, Tucson, AZ, USA

6 Comrod, Tau, Norway

7 Planetary Science Institute, Tucson, AZ, USA

8 Norwegian Polar Institute, Tromsø, Norway

9 Cornell University, Ithaca, NY, USA

10 Jet Propulsion Laboratory, California Institute of Technology, Pasadena, CA, USA

11 Dresden Technische Universität, Dresden, Germany

shallow imaging down to several meters, and a reduced bandwidth of the lower frequencies (center frequency 375 MHz) will be used for imaging deeper structures. The majority of data will be collected at regular distance intervals whenever the rover is driving, in each of the deep, shallow, and surface modes. Stationary measurements with extended integration times will improve depth range and SNR at select locations. The RIMFAX instrument consists of an electronic unit housed inside the rover body and an antenna mounted externally at the rear of the rover. Several instrument prototypes have been field tested in different geological settings, including glaciers, permafrost sediments, bioherme mound structures in limestone, and sedimentary features in sand dunes. Numerical modelling has provided a first assessment of RIMFAX's imaging potential using parameters simulated for the Jezero crater landing site.

Keywords Mars · Perseverance · Rover · GPR · RIMFAX

1 Introduction

The Radar Imager for Mars' Subsurface Experiment (RIMFAX) is part of the payload for NASA's Mars 2020 *Perseverance* Rover (Farley et al. 2020, this issue). RIMFAX will add a new dimension to the rover's toolset by providing the capability to image the shallow subsurface beneath the rover The principal goals of the RIMFAX investigation are to image subsurface structure, and to provide information regarding subsurface composition. The data provided by RIMFAX will aid the Mars 2020 rover in its mission to explore the ancient habitability of its field area, and select a set of promising samples for analysis, caching, and eventual sample return.

Ground Penetrating Radar (GPR) is a non-invasive geophysical method that is a popular tool in sedimentology, glaciology, archaeology, and utility mapping (Daniels 2004; Jol 2008). A GPR is made of an electronics unit and an antenna. The radar transmits radio frequency electromagnetic waves into the subsurface, typically operating in the 10–1000 MHz band. Changes in the subsurface dielectric properties result in the reflection of part of the propagating wave back to the antenna. Figure 1 gives an illustration of RIMFAX mounted on the Mars 2020 rover traversing the Martian surface. The result is an image of the subsurface shown in the lower part of the figure.

GPR measurements are based on the recorded time between transmission of a wave and reception of the reflected/refracted return wave, called the two-way travel-time. Knowing the wave velocity in the ground, the depth to the reflector, d, can be calculated by: $d = vt/2$, where v is the wave velocity in the subsurface and t is the two-way travel-time. The GPR collects regular subsurface soundings as it moves laterally along the surface. Displaying successive soundings adjacently in a diagram creates a 2D image of the subsurface called a GPR profile, or radargram.

When the geological materials have a low loss tangent value the wave velocity in the ground is determined by the real part of the material's permittivity, ε', which is mainly controlled by density in dry rock and regolith (see later section). The time-depth resolution of GPR is considered equivalent to the radar wave's pulse length, or approximately the inverse of its frequency bandwidth, B. The depth resolution in meters depends on the wave velocity, and is given as: $\Delta d = v/2B$.

The Report of the Mars 2020 Science Definition Team (Mustard et al. 2013) suggested that a ground penetrating radar instrument might be valuable for revealing subsurface stratigraphic relationships that could be correlated with surface outcrops. They envisioned that

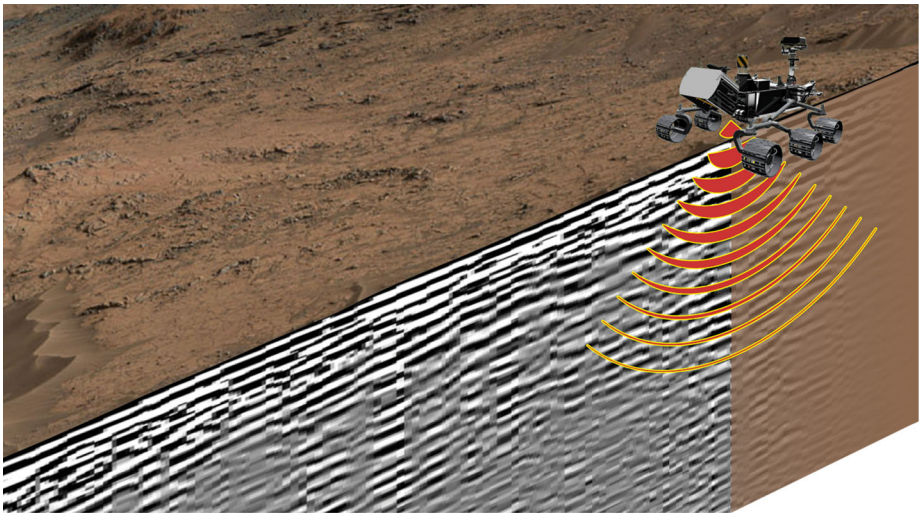

Fig. 1 Artistic illustration of the Mars 2020 Perseverance rover traversing the surface of Mars, including RIMFAX transmission of radar waves into the subsurface and visualization of subsurface geomorphology and layering in collected data

the radar would be used to augment rover surface operations by providing a continuous cross-section of the subsurface. In 2014, RIMFAX was selected by NASA as one of seven instruments for the Mars 2020 rover. A RIMFAX flight model and a complete flight spare was fabricated, and the flight model was delivered to the rover for integration in 2019.

RIMFAX traces its heritage to a series of ground penetrating radars developed for sounding polythermal glaciers with different frequencies to infer the thermal state of the glaciers (Hamran and Aarholt 1993; Hamran et al. 1996; Ødegård et al. 1997) and studying ice shelves in Antarctica (Hamran et al. 1998). Later and ultra wideband version was developed as a prototype for the WISDOM radar on the ExoMars mission (Hamran et al. 2008) and later also used for medical imaging (Brovoll et al. 2014).

Mars was first observed with Earth-based radar in 1963 (Goldstein and Gillmore 1963). Subsequent Earth-based imaging revealed strong radar echoes from the south residual polar cap, as well as a large equatorial region near the Tharsis volcanoes that exhibits almost no radar reflectivity dubbed "Stealth" (Muhleman et al. 1991). The European Space Agency's Mars Express Orbiter includes the MARSIS synthetic aperture radar capable of sounding in four bands between 1.3 MHz and 5.5 MHz with a 1 MHz bandwidth (Jordan et al. 2009). NASA's Mars Reconnaissance Orbiter includes the SHARAD synthetic aperture radar capable of sounding at 20 MHz with a 10 MHz bandwidth (Jordan et al. 2009; Flamini et al. 2007). These orbital radar systems have detected subsurface structures in Martian mid-latitude regions (Watters et al. 2007), extensive layering in Mars' polar ice deposits (Plaut et al. 2007), and potential evidence for a lake 1.5 km beneath the south polar layered deposits (Orosei et al. 2018).

There have been published several studies and field work showing the scientific potential of imaging the subsurface of Mars from a rover (Grimm 2003; Heggy et al. 2006; Grant and Schutz 2003). The WISDOM GPR on the ESA ExoMars rover was selected in 2003 and is planned to launch in 2022 (Ciarletti et al. 2011, 2017).

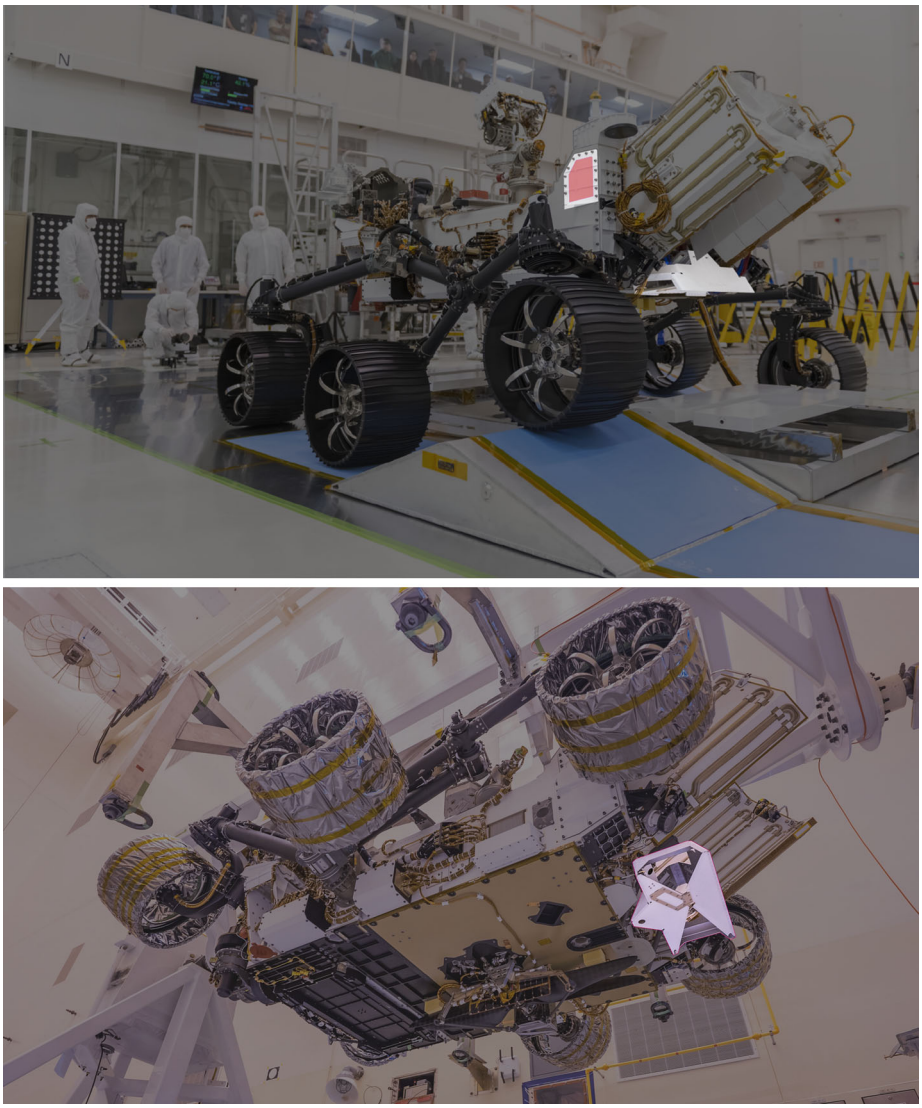

Fig. 2 Top: Location of RIMFAX electronics box within left aft tower (red highlight) of Mars 2020 rover and RIMFAX antenna at lower aft. Bottom: Clearer view of RIMFAX antenna (white highlight), looking up at underside of suspended rover. Original image a courtesy of NASA/JPL-Caltech

As part of the *Perseverance* rover payload at Jezero Crater, RIMFAX will have a unique opportunity to explore the Martian subsurface. Sounding from close proximity to the surface from a mobile surface vehicle will provide RIMFAX with the potential to acquire radar data with much higher horizontal and vertical resolution than can be achieved from Earth or from Mars orbit. This, combined with the availability of a wide range of geological context data from the *Perseverance* rover payload as a whole should provide an excellent opportunity to assess the applicability of ground penetrating radar as a tool for *in-situ* planetary exploration generally.

2 Science Objectives

The principal science goals of the RIMFAX investigation are to image subsurface structure, and to provide information regarding subsurface composition. The landing site at Jezero crater has been studied in great detail from orbit, and additional and new results are changing our geological conception of the area regularly (e.g. Goudge et al. 2015, 2018; Horgan et al. 2019; Brown et al. 2018). RIMFAX will provide important insight into the subsurface stratigraphy of the landing site and traverse path, and current knowledge of the crater can provide insight into what sedimentary sequences might be observed by the radar.

2.1 Basin Ejecta and Crater Fill

The Isidis impact ($D = 1900$ km) occurred in the Noachian era, ~3.95–3.97 Ga (Schultz and Frey 1990; Mustard et al. 2009; Werner 2008), and whether the impact was subaqueous or subaerial is a matter of debate. Related extensive breccias and impact melts have been noted (Mustard et al. 2007; Mustard et al. 2009), as well as fluvial channels and a mineralogy that indicates past aqueous alteration (Fassett and Head 2005; Ehlmann et al. 2011). The NW margin of this basin formed the target area for the much smaller Jezero impact ($D = 45$ km).

Jezero was originally a complex crater (Melosh 1989; Barlow 2006) with a central peak, but it was severely deformed and eroded after impact. The Jezero impact most likely created large amounts of fractured debris (such as scree, or talus), mass flows, density currents and melt rock during the crater excavation and modification stages, comparable to terrestrial aqueous impact craters (Dypvik and Kalleson 2010; Dypvik et al. 2018). The relationship between Isidis and Jezero impactites and their relative contributions to these units, however, is not clear.

2.2 Deltaic and Paleolake Deposits

The deltaic deposits of western Jezero crater will be the initial focus of Mars 2020 operations. The timing of the Jezero crater lake(s) is highly uncertain, as is the thickness of the delta and lake sediments relative to other crater infill materials. The Jezero impact and deltaic deposition ages are constrained by the formation of the Isidis impact and by a crater floor unit that may be stratigraphically higher (discussed below). Fassett and Head (2005) suggested a date of 3.8 ± 0.1 Ga for the end of fluvial activity in Jezero based on the cessation of valley networks that feed the basin and the lake may have lasted for millions of years (Schon et al. 2012).

There is an extensive history of using ground penetrating radar systems to study both modern and ancient deltaic environments. Various sedimentary processes lead to different lithofacies that are distinguishable by radar, allowing for mapping of different units over large distances. For example, Olariu et al. (2011) used GPR and 3D analysis techniques to map distributary channels in delta deposits in Cretaceous sandstones in Utah. In this case the GPR profiles were also linked to a high-resolution topographic map of the surface to trace visible units into the subsurface, a technique that we will also be able to use with RIMFAX. Lee et al. (2005) performed a similar GPR study on an Upper Cretaceous delta in Wyoming and were able to measure the position and volume of prograding bar deposits.

RIMFAX will reveal layering within the delta and may provide critical information about its evolution, including possibly its vertical extent and the position of channels through time. It will also be able to detect possible lake sediments, which will shed light on the evolution of the fluvial system as a whole. It is also of great interest to see if RIMFAX

can detect the previously mentioned scree/mass flows and/or crater-floor melt rocks beneath the delta successions, as well as possible parautochthonous impact breccias/megabreccias. This would give new dimensions to our understanding of the Jezero impact and succeeding crater-filling events.

The fluvial systems exterior to Jezero and towards Northeast Syrtis are also of great interest, and may potentially be accessible later in the Mars 2020 mission.

2.3 Clay and Carbonate Sequences

The likely wetter and warmer Noachian era is probably the period when most chemical weathering and alteration happened on Mars, and there should be detectable resulting deposits and formations within the Jezero crater filling sequences (Sætre et al. 2019). The smectites and Mg- carbonates of the western fan are most likely detrital minerals (Ehlmann et al. 2011). These lithologies will be among the main targets in the Mars 2020 search for biosignatures and will be an important focus of RIMFAX.

2.4 Crater Floor Units

The so-called dark-toned mafic crater floor is one of the most enigmatic parts of the Jezero stratigraphy. The floor has a CRISM-derived spectral signatures of olivine and pyroxene (Goudge et al. 2012) and has crater age dates ranging from $3.45 + 0.12/ - 0.67$ Gya (Neukum system, Goudge et al. 2012), to 2.6 ± 0.5 Ga (Hartmann system, Shahrzad et al. 2019), to 1.4 Gya (Hartmann system; Schon et al. 2012). It is likely that this unit was deposited after the deposition of the lake and delta, and (Schon et al. 2012) document embayment of the delta by the floor unit, suggesting the delta may have partially eroded prior to deposition of the floor material. The dark-toned unit is $\sim$10 m thick near the edges of the deposit (Goudge et al. 2015; Shahrzad et al. 2019), which is most likely well within the penetration depth and resolution of RIMFAX.

While the dark-toned floor unit looks uniform at large scales, closer inspection at HiRISE scales (tens of cm/pixel) reveals it to host several surface textures (Cofield and Stack 2017; Shahrzad et al. 2019). It has distinct topographic expression at its edges and overlies a lighter-toned deposit that can have polygonal fractures (Shahrzad et al. 2019). The dark-toned unit lacks wrinkle ridges and has been interpreted as a lava flow, ash deposit or mafic sandstone (Goudge et al. 2012; Schon et al. 2012). Radar is very sensitive to differences in rock density and RIMFAX should be able to determine the properties of this deposit and distinguish between lava flows, melt rock and other types of sedimentary volcanics.

Alternatively, we suggest that these units may be melt rock, ejecta and suevites from the Jezero, or even the Isidis, impact. In this case, these mafic layers could also be characterized by RIMFAX, since impact melts would most likely be denser and heavier than lavas formations. RIMFAX has great potential to reveal layering within the upper part of the crater floor and determine the emplacement processes of this material and its relationship to the fluvial systems in the crater.

2.5 Dielectric Properties

The interaction of radar waves with target materials is governed by the materials' dielectric permittivity. The permittivity is an intrinsic property that arises from the polarizability within the target material. It is commonly expressed as a complex quantity:

$$\varepsilon = \varepsilon' - i\varepsilon''$$

The relative permittivity is defined as

$$\varepsilon_r = \varepsilon/\varepsilon_0$$

where ε_0 is the permittivity of free space. The real part of the relative permittivity, ε_r', often called the dielectric constant, controls the speed of a radar wave in the material, as

$$v = c/\sqrt{\varepsilon_r'}$$

and the imaginary part of the relative permittivity, ε_r'', referred to as the dielectric loss, determines the rate of attenuation of the signal as it propagates through the material, or the "loss." The "loss tangent," defined as

$$\tan\delta = \varepsilon''/\varepsilon'$$

is a commonly-used quantity that is particularly useful for comparing the penetration potential of radar signals into different materials. The imaginary part, and therefore, the loss tangent, is commonly strongly dependent on frequency.

On Earth, liquid water is the most important factor controlling variations in dielectric permittivity, both due to the polarizability of the water molecule and to the ability of water to host conductive species. In the absence of liquid water, the real part of the permittivity, ε', is approximately constant for most geological materials over the radar frequency range (Campbell and Ulrichs 1969; Ulaby et al. 1990), and is largely controlled by density. Empirical relationships between the bulk density of particulate mixtures like those that characterize the regoliths of the Moon and other bodies have been derived from measurements of powdered and solid samples at a range of frequencies; they generally follow the form

$$\varepsilon' = a^{\rho}$$

where ρ is the bulk density of the material and the constant a has a value close to 2.0 (see references in Hickson et al. 2018, Table 1). Therefore, solid, indurated materials have higher values of dielectric constant than do low density / high porosity fragmental materials, and thus show slower radar wave propagation. The dielectric loss (via the imaginary part of the permittivity) in the absence of water is largely controlled by composition, with each material or mixture of materials exhibiting a unique frequency-dependent loss profile. This arises via the electrical conductivity of the material, to which the imaginary part is directly proportional. The magnetic permeability, μ, also affects radar interactions with some materials containing a significant magnetic component (e.g., Stillman and Olhoeft 2008; for most geological materials, however, μ does not play a significant role.

A radar signal decreases in power as an exponential function of distance travelled through a material, moderated by the dielectric loss. For GPR, subsurface contrasts in dielectric permittivity give rise to radar reflections. These contrasts are usually associated with geological units, which have variations in density and/or composition. The strength of a given reflection is a function of the magnitude of the dielectric contrast. Each reflection produces an additional signal attenuation, so that the ultimate penetration potential of a given signal depends on the number and strength of reflections along the signal path. For geological settings in which a large number of scatterers, such as buried boulders, are present, the ultimate penetration depth is smaller than a setting characterized by a few continuous layers. The volume scattering loss may be larger than the conductivity or dielectric loss in the martian subsurface (Grimm et al. 2006).

Table 1 List of a selection of buried geological features that RIMFAX can investigate

Geologic features and environments potentially detectable by RIMFAX			
Buried geological feature	Ancient climate & habitability significance	Observable characteristics	RIMFAX signature
Stream Channels	Warm and wet	Gravel beds; Topography; Meander & drainage forms; Cross-bedding zones	Sharp density transition; Block scattering; May require plan-view grid
Sedimentary Bed–Lacustrine	Warm and wet	Level periodic layers; Few internal rocks	Closely spaced parallel reflectors; Level structures
Sedimentary Bed–Aeolian	Dry	Cross bedding; Stoss and lee slopes	Closely spaced dipping reflectors; Asymmetric 3-D structure
Unconformaties	Variability	Layer discontinuities	Truncated reflector sequences
Subaerial Mantle	Dry	Fine grained & mostly rock free; Drapes substrate	Irregular sub-mantle surface; Few point scatterers in overburden
Glacial/Periglacial	Cold and damp	Regolith sorting; Network patterns; Till structure	Hyperbolic reflector (block) distribution; Paleosurface topography
Ice	Relic deposits Preserve organics	Ice layer; Proximity to caprock and other layers	Subjacent hyperbolic reflectors, wave velocity; Internal reflectors in layer
Water/Brine	Past and/or Current habitat	Proximity to caprock/ice; Estimated temperature	Strong reflections; Subjacent hyperbolic reflectors, wave velocity; Polarity
Volcanic	Hydrothermal	Sub-vertical, cross cutting or horizontal dense rock	Density transition; Truncations; 3-D structure; horizontal reflector packets
Impact Craters	Paleosurface age; Hydrothermal	Unsorted blocks; Deformed strata; Melt sheet	Abundant blocky reflectors; Deformed layers; Laterally extensive reflectors
Regolith Thickness	Geological history	Basement bedrock transition-zone structure	Basal reflector; Change in hyperbolic reflections with depth

Few laboratory measurements of the permittivity values of Mars-relevant materials have been conducted. Stillman and Olhoeft (2008) performed measurements on various Mars regolith analog materials, including hematite and magnetite, and Cunje et al. (2018) reported on measurements at Martian temperatures of smectite clays chosen to represent materials likely to be present at the Jezero landing site. In the absence of liquid water, the inherent

permittivity values, and their frequency dependence, measured by these workers provide a context in which to interpret RIMFAX data from Jezero crater.

The depth of a given reflection can be determined if the real part of the permittivity of the overlying materials is known. Comparison of reflections with identical time delays in areas with different material properties can be ambiguous, since the speed of the radar wave varies with permittivity. The permittivity determines the radar wave velocity in the ground. A radar measures the distance in two-way-traveltime and the wave velocity is needed to convert the measurements to depth. There is a technique used on Earth called normal move out that uses the GPR to measure the wave velocity in the ground. Separate transmitter and receiver antennas are needed and radar measurements are taken successively when the transmitter and receiver antennas are moved away from each other. If several layers are seen in the radar data the velocity as a function with depth can be estimated. RIMFAX has only one antenna that is used both for transmitting and receiving and normal moveout processing cannot be used.

If point scatterers are observed in the subsurface by the radar, a similar processing as done for the normal moveout geometry can be used. The two way traveltime history as a function of distance traveled by the radar will be a hyperbolic function. The distance traveled by the radar on the surface is known, then the position and shape of the hyperbola can be used to determine both the depth to the reflector and the average velocity in the ground above the reflector. If several point reflectors are seen in the radar image, the two dimensional velocity map can be estimated.

The depth resolution is depending on the transmitted bandwidth, the radar velocity in the ground and the type of window function used when transforming the radar data from frequency to time domain. For the RIMFAX high resolution shallow mode the depth resolution will vary from 10 cm for a permittivity of 9, to 20 cm for a low permittivity of 2. For the deep mode the depth resolution will vary from 20 to 40 cm. The depth resolution tells us how close two reflecting layers can be, and still be resolved as two distinct layers. Interfaces thinner than the depth resolution can still be detected by the radar, but multiple interfaces below the depth resolution will not be resolved.

The RIMFAX antenna is located at 60 cm above the martian surface. The RIMFAX radar can therefore get an estimate of the surface reflection from the air to the martian surface. If the surface roughness height is smooth compared to the radar wavelength the reflection strength is determined by the permittivity of the surface through the Fresnel reflection coefficient. From measuring the surface reflection strength, the permittivity of the shallow subsurface can be estimated and thereby the density of the ground. This will give the relative variation in surface density along the rover travers.

RIMFAX will also collect measurements while the rover is stationary. Collecting time lapse soundings over a diurnal cycle enables the possibility to study changes in the surface reflection coefficient with time. The surface reflection coefficient depends on the surface permittivity that may change with the interaction between the atmosphere and the martian ground. If shallow reflectors are seen in the radar trace, the phase and amplitude of the propagation through the shallow subsurface can be analyzed and variations in the permittivity and dielectric loss may be studied. Such measurements may provide information about diurnal interactions between water vapor in the atmosphere and the ground.

2.6 Water Ice and Brines

The current Martian environment supports a range of atmospheric, surface, and subsurface volatiles. The distribution of these volatiles is controlled by pressure and temperature, as well as a multitude of additional chemical and physical processes—all of which

vary on durnal, seasonal, interannual, and climatic timescales. The *Perseverance* landing site in Jezero crater at 18° N latitude, and −2.6 km altitude was chosen partially for its mild seasonal and diurnal temperature variations. It is therefore anticipated that near-surface ground ice in equilibrium with present atmospheric conditions, and transient pure liquid water, which are common at higher latitudes (Piqueux et al. 2019; Richardson and Mischna 2005), should generally be absent. However, as with everywhere on Mars, temperatures at depth at Jezero crater are well below 0 °C, so deeply buried ice deposits formed during past climatic epocs could still be present today as long as they are sufficiently isolated from the atmosphere (Clifford 1993; Dundas et al. 2018). If present, thick subsurface layers composed of pure water ice are detectable by ground penetrating radar because of their lower dielectric constant and lower attenuation compared to soil.

As described earlier, the presence of pure liquid water, or liquid water containing dissolved ions is readily detectable by ground penetrating radar due to its high dielectric permittivity. At martian mid-latitudes, there is a strong theoretical case for the presence of near-surface transient brines (Martínez and Renno 2013; Jones 2018), as well as evidence for the presence of brines today at Gale Crater (Martín-Torres et al. 2015). RIMFAX has the potential to detect the presence of near-surface transient brines by monitoring temporal changes in the dielectric properties of the surface while stationary. Additionally, shallow aquifers containing brines have been suggested to be responsible for a range of geomorphic features on Mars (Mellon and Phillips 2001; Goldspiel and Squyres 2011; Gaidos 2001; Chevrier and Rivera-Valentin 2012). While the nature and prevalence of such aquifers is presently not well established, the detection of a strongly reflecting continuous subsurface layer by RIMFAX would potentially indicate their presence.

2.7 Ice and Periglacial History

The modern martian climate (Amazonian up to the present) has been marked by subfreezing conditions and dominated by glacial and periglacial processes. Ice-related landforms are commonplace at middle and high latitudes e.g., (Squyres and Carr 1986; Milliken et al. 2003; Mangold 2005), but due to the warmer and drier conditions, surface and near-surface water ice are not presently stable in the region of Jerezo Crater.

The precise nature of the ancient climate at Jezero is as yet unclear. Liquid water was certainly present in the distant past suggesting warmer and wetter conditions. Was this liquid water still present as the ancient climate cooled to that of the present day? Were surface ice and frozen soils common in ancient times while liquid water eroded the channels, filled lakes, and deposited deltas? Were there cycles of freeze and thaw? Additionally, could more recent orbit and climate oscillations allowed for near-surface water ice to persist in this region for extended periods of time, perhaps as recently as ∼0.5 My ago (Mellon and Jakosky 1995; Chamberlain and Boynton 2007).

These ice occurrences (distant past or recent) may have left signatures imprinted on the paleosurface, perhaps now buried, that may be detectable today as semi-regularly-spaced and sorted rock and soil structures, unsorted till deposits, and buried relic-ice deposits. Horizontal and vertical patterns in the concentrations of cobbles and boulders relative to regolith fines, buried massive-ice deposits, and ice-saturated soils can be detected by RIMFAX, and help diagnose paleoclimate conditions.

2.8 Regolith Development and Properties

Bedrock structure and lithology typically dominate observations of martian landforms on length scales >100 m. On smaller scales relevant to a lander or rover, the martian

surface is largely blanketed by a layer of regolith. This regolith forms by the physical and chemical breakdown of local bedrock, combined by erosion and aggradation of sediments through aeolian, fluvial, mass wasting, and impact processes (Ollier and Pain 1996). The thickness and makeup of the regolith captures the history of these competing processes of formation and transport. The depth to the martian megaregolith and fractured basement is largely unexplored, and holds clues to the crustal porosity profile, overburden compaction, and the holding capacity of the cryosphere (Clifford 1993; Hanna 2005). RIMFAX can potentially address many of these issues by observing the depth of the porous regolith and the transition to bedrock, the distribution of clasts of bedrock fragments, and the presence of horizons and discontinuities.

On shallower decimeter scales, the regolith at every past Mars landing site has been observed to exhibit horizons of loose fines, dust mantles, and weakly cohesive crusts (Arvidson et al. 1989; Shaw et al. 2009; Sullivan et al. 2011; Edgett et al. 2013). While dielectric contrasts between these layers may be minimal, thermal contrasts may reveal the presence of these distinct layers (Mellon et al. 2008). RIMFAX passive mode will observe microwave thermal emissions integrated from the subsurface layers. The frequency dependence of emissions can be used to estimate the subsurface temperature profiles from which subsurface thermophysical properties can be inferred e.g., Muhleman (1971), Keihm (1984), Montopoli et al. (2011).

3 Instrument Design

3.1 Requirements

Requirements for the Mars 2020 mission and rover payloads are divided into five levels. Level 1 is the top level covering the complete mission, including bringing a rover to Mars, restrictions on where to land on Mars, total rover drive distance, sample and cache capability, contamination control, planetary protection, and more. The Level 2 requirements relevant to the performance of RIMFAX as a scientific instrument include requirements on the Mars 2020 payload system to be able to survey scenes for geologic content, interpret geologic processes, and accommodate RIMFAX.

All instruments are to meet Level 3, 4 and 5 requirements. These levels include requirements on science, electrical and mechanical interfaces, environment, EMI/EMC, contamination control, planetary protection, and more. The science requirements relevant to the RIMFAX design and capabilities are shown in Fig. 3, and written out in Table 2 for Level 4. The science requirements imposed on RIMFAX all lead up to the Level 3 requirement (L3-01) which states that the Payload System shall have the capability to map subsurface geological layers to a depth of at least 10 m along the rover traverse path. L3-01 is automatically met when all L4 requirements in Fig. 3 are met. Level 5 requirements are not shown in Fig. 3.

The performance of RIMFAX was referenced to a subsurface model of a dense, intermediate-loss basalt (3.00 g/cm^3, $\varepsilon_r = 7.06 + i0.247$) overlain by a 10 meter thick basaltic regolith (1.60 g/cm^3, $\varepsilon_r = 2.84 + i0.014$) with a scattering loss of about the same strength as the dielectric loss. To be able to verify performance requirements, transmission line test kits were developed to simulate the conditions for which the requirements were given.

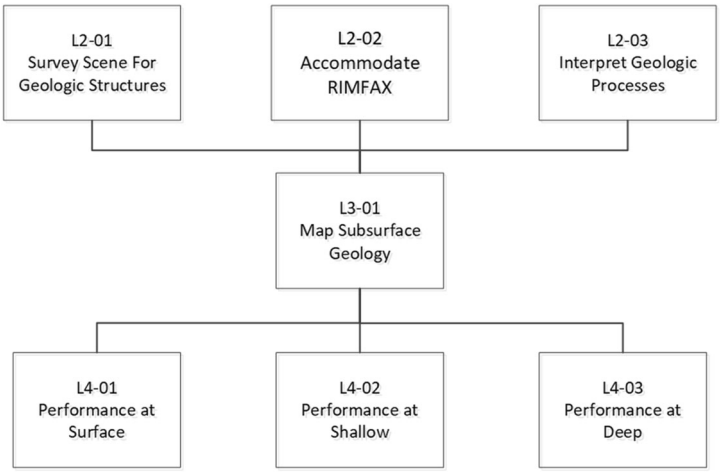

Fig. 3 Flow chart of science requirements relevant to RIMFAX design and capabilities, from Level 2 through Level 3 down to Level 4

Table 2 Level 4 Science requirements relevant to RIMFAX design and capabilities

Requirement	Description
Performance at Surface	RIMFAX shall have the capability to measure the surface reflections
Performance at Shallow	RIMFAX shall have the capability to measure a sub-surface reflection 30 cm below the surface with a signal strength of −27 dB below the surface reflection
Performance at Deep	The RIMFAX investigation shall detect subsurface layering with a permittivity contrast of 20% in unconsolidated regolith down to 10 meter depth having a total link loss of 100 dB

3.2 Waveform

Commercial GPR systems used on Earth normally employ time-domain impulse signals. The receivers in these systems are very often time-repetitive sampling receivers (Daniels 2004). It has been shown that this type of waveform sampling is not optimal regarding power consumption and dynamic range (Hamran 1995, 2010). For this reason a Step Frequency (SF) waveform was chosen for the WISDOM GPR (Ciarletti et al. 2017). The SF waveform has some inherent problems and the most difficult of these is the range ambiguity that results from the discrete sampling of the waveform in the frequency domain. We have therefore chosen a Frequency Modulated Continuous Wave (FMCW) waveform for the RIMFAX radar. In FMCW radar the baseband signal is low-pass filtered before being sampled. This filter effectively removes deeper reflectors and yields an ambiguity-free range interval. It has also been shown that the FMCW waveform is more energy efficient than the SF waveform (Hamran 2010). The RIMFAX FMCW waveform uses a gating technique that allows a single antenna to be used both as a transmitter and receiver.

Table 3 Main parameters of the RIMFAX instrument with typical values

Parameter	Programmable	Symbol	Typical value
Start frequency	*	F_1	≥150 MHZ
Stop frequency	*	F_2	≤1200 MHz
Maximum bandwidth	*	B	1050 MHz
Output power	*	P_T	−18 dBm to +13 dBm
Receiver channel gain	*	G_{Rx}	23 dB to 54 dB
Beat frequency Bandwidth		B_{bf}	29 kHz
Noise Factor		NF	<6 dB
Gate frequency	*	F_G	≤12.5 MHz
Sweep time	*	T_S	≤100 ms
Power consumption		P_0	2.5 W (Idle)
		P_M	9.5 W (Sounding)
Mass		M_{EU}	1245 g
Size		W, L, H	135, 194, 66 mm

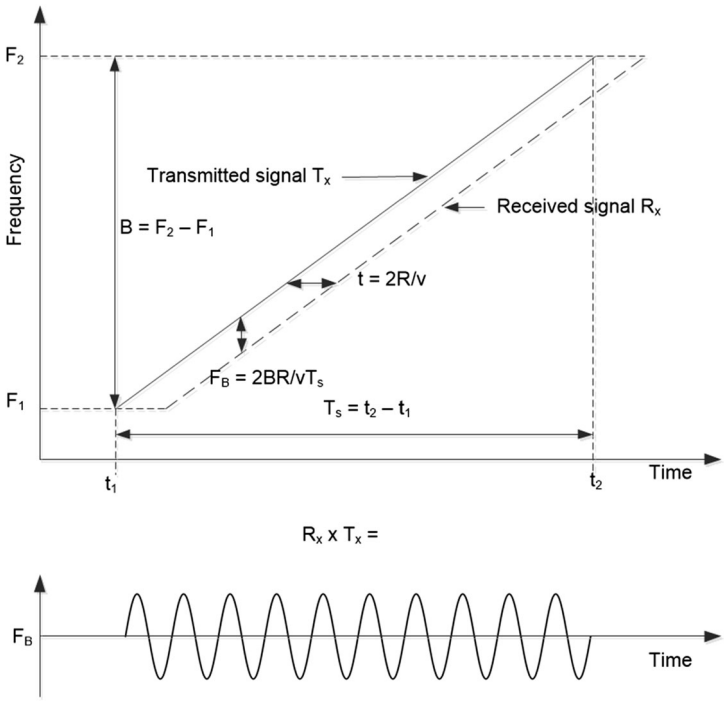

Fig. 4 Illustration of FMCW radar operation principle. Transmitted frequency-swept signal is multiplied with delayed received signal to make a baseband signal. Frequency of baseband signal is directly proportional to delay time and to distance from radar to reflector

The working principle of an FMCW radar is illustrated in Fig. 4, and Table 3 gives the main paramaters characterizing the radar. A signal swept through frequencies F_1 to F_2 is

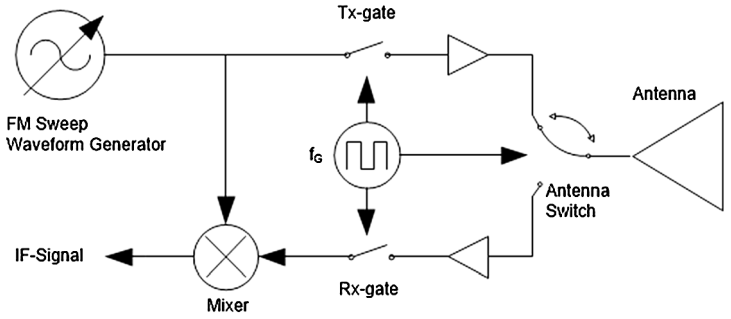

Fig. 5 Block diagram of basic elements in the gated FMCW radar of RIMFAX

transmitted through the antenna. A signal reflected from a distance, d, and delayed by the two way travel time, t, given by $t = 2d/v$, is received by the antenna. The received delayed signal will have a different frequency than the signal currently being transmitted. Multiplying the received signal with the signal currently being transmitted will give a baseband signal with a frequency equal to the frequency difference between the two signals. For a stationary reflector this frequency difference will be constant over the sweep. The frequency of this signal, called the beat signal, will be proportional to the delay time, and thereby the distance range, to the reflector. The proportionality constant is given by the ratio between the sweep bandwidth and the duration of the sweep. The frequency of the beat signal is given by:

$$f_b = 2Bd/vT_s$$

where $B = F_2 - F_1$ is the sweep bandwidth, T_s is the sweep duration, v is the wave velocity in the material and d is the range to the reflector. Measuring the beat frequency thus yields the range to the reflector. The amplitude of the received sine-wave signal will give us the reflection strength. If several reflectors are present the baseband signal will be a summation of all the different reflected signals. Spectral estimation techniques like Fourier transforms can calculate the reflected signal.

3.3 Gating

The FMCW signal is gated in a switch before being amplified and fed to the antenna through the antenna switch, see Fig. 5. The gating switches the FMCW signal on and off with a duty cycle up to 50%. The gating frequency is much lower than the transmitted-signal frequency and higher than the baseband signal spectrum. The reflected signal response will be a convolution between the gated, square-wave transmitted signal and the square wave of the receiver gating. This response function will be a triangular waveform producing an effective linear gain on the received signal as a function of depth, see Fig. 6 (Hamran 1995). Typically the maximum of the gating function will correspond to the maximum instrumented range. After the gating peak a linear reduction in amplitude will be combined with the spherical loss and attenuation in the media reducing the reflected signal rapidly.

If the receiver gating waveform is turned on with a slight delay after the transmitter gating signal turns off, there will be a time window where no signal is entering the receiver. This is illustrated in Fig. 6, in which the receiver gate-signal delay is represented by T_R. Any reflected signal from the exterior or subsurface that arrives during the time-delay window from 0 to T_R does not enter the receiver. The radar response as a function of delay time will

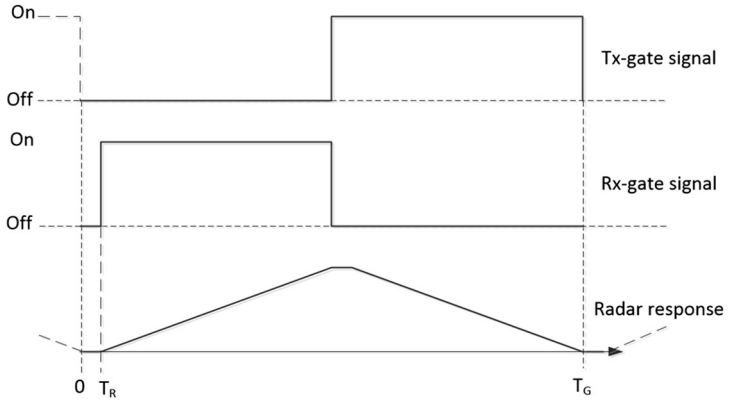

Fig. 6 Diagram of RIMFAX gating sequence and net effect on gain. Radar response is the convolution of transmitter gating signal and receiver gating signal. Response has a triangular shape, giving linear gain with depth

then be a symmetric triangular shape with a flat-peaked top of length T_R at time at $T_G/2$, giving a linear gain with travel time and depth. If the frequency of the square wave gating signal is F_G, the total gating window length is $T_G = 1/F_G$.

The gating makes it possible to remove strong reflectors from the receiver signal before the signal is digitized, effectively increasing the dynamic range coverage of the radar system.

3.4 Design Considerations

The RIMFAX instrument consists of two main subsystems, the electronics unit and the antenna. The electronics unit (EU) resides inside the left aft tower of the rover in a benign, thermally controlled environment, while the antenna is located under the hot RTG facing down to the cold ground (Fig. 2). This results in a large thermal gradient over the antenna that puts heavy constraints on its design.

3.5 Electronics Unit

The main performance requirements (Fig. 3) were used as input for the design and implementation of the instrument. The radar must detect structures close to the surface with good resolution, and at the same time have a high dynamic range to see deep into the ground. This is achieved by executing several soundings in different modes at each position along a rover traverse.

Since ground composition on Mars (i.e., porosity and the dielectric properties) is largely unknown, the features of the radar are programmable. This allows us to configure the radar depending on what we see on Mars and what we want to investigate. The configuration/setup can be changed for every sounding.

The EU (Figs. 7, 8) is connected to the rover with two 15p HD DSUB for communication with the rover, one for each Rover Compute Element (RCE). The interface is RS-422/UART, with a rate of 155 kilobaud. There is one 9p DSUB for the voltage supply, since the supply from the two RPAMs are ORed outside of the instrument. The EU has two RF connectors, one to the antenna and one to the calibration cable, which is coiled up inside the rover body. It is used for monitoring the health of the instrument, for tracking of long term stability and for calibration of the radar.

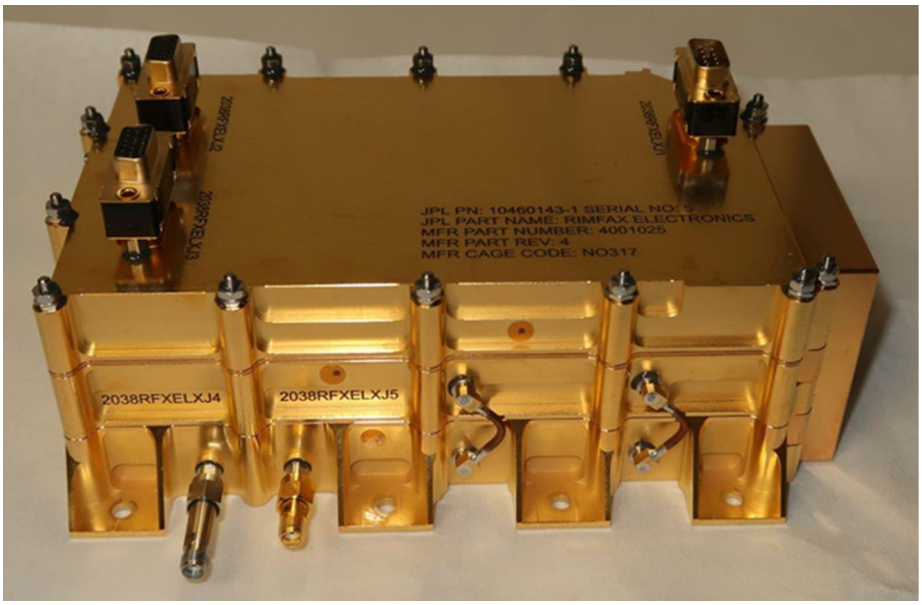

Fig. 7 Photo of RIMFAX electronics unit Flight Model SN5, taken in a clean room after the TVAC test. DSUBs for communication and voltage supply visible on top, SMA antenna port and calibration port visible on front, all with connector savers installed

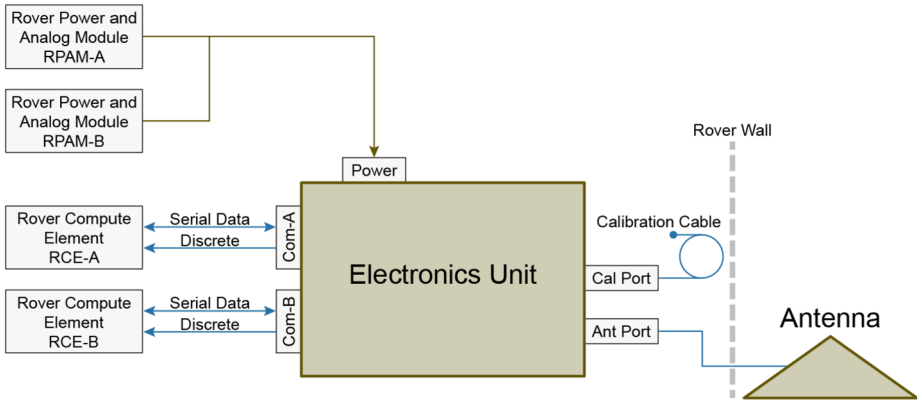

Fig. 8 Block diagram of RIMFAX instrument with connections for rover voltage supply, rover communication, and signal ports

RIMFAX is a low power-consumption instrument. It has two power states, Idle and Sounding. In Idle only the logic is powered on, so that it can communicate and receive commands from the RCE. When commanded to do a sounding, the instrument switches on the supply voltages for the RF and analog sections. Depending on the duty cycle of the soundings, the average power consumption can be very low, less than 5 W for a typical traverse.

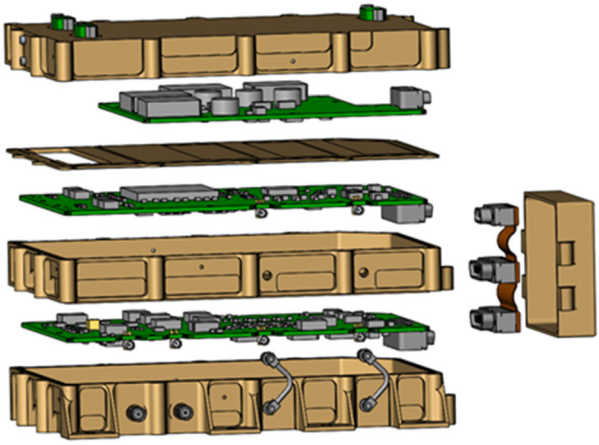

Fig. 9 Exploded view of RIMFAX electronics unit with printed circuit boards. From top to bottom, sections are: power-DC board with connectors for voltage supply and communication; shielding plate; data control board; RF-analog board. Flexprint with three connectors to the right is the backbone bus. Right-most element is the lid to protect the bus

During thermal vacuum (TVAC) testing the power consumption during sounding was less than 9.5 W in nominal conditions ($T = +20$ °C, voltage supply = 28 V) and a maximum of 10.2 W in worst case conditions ($T = +55$ °C, voltage supply = 36 V). Due to the low power consumption, temperature is not an issue. In the TVAC we measured temperatures on the printed circuit boards that were 2–6 °C above the maximum temperature on the EU mounting interface. This was measured while the instrument was in an operational mode and at maximum hot temperature.

This wide bandwidth provides significant benefits: low frequencies allow us to see deep into the ground, while high frequencies give good resolution of shallow reflectors. The maximum instrumented range (i.e. the depth to which the radar is configured to measure) is determined by the bandwidth and sweep rate, and may be set between 5.4 m to almost 1 km in free space. For normalization purposes the total sweep time, and hence signal collection time, for all soundings is held constant, at 100 ms. Should a shorter sweep be required, it is run several times until 100 ms is reached, and the resulting sounding is an average of measurements made over this time. A particular window within the instrumented range can be recorded by setting the gain and the gating parameters (see later section on modes).

The EU (Figs. 9, 10) consists of three separate boards: one DC/DC converter board, one data control board and one RF analog board. The backbone bus between the boards is implemented with a vertical flexprint. Two short coaxial cables on the outside of the box are used for the RF and analog low-noise signals.

All the logic is implemented in a Microsemi RTAX2000SL FPGA. The FPGA contains logic for two UART modules, for monitoring the health of the instrument (housekeeping), for generating and controlling the output frequency sweep, for controlling the gating and for data collection.

Two communication interfaces, one for each of the rover computers, are required. The communication block receives commands from the rover and transfers back sounding results and status of the instrument, including housekeeping data. Housekeeping is done with two 8-channel, 12-bit ADCs that monitor all the voltages and the temperatures on the boards.

When the FMCW radar receives an echo from the reflector the echo is homodyned (mixed) with a replica of the transmitted waveform to produce a beat signal. The frequency of this beat signal depends on the distance (range) to the reflector and the sweep rate of the waveform. Since we want to control the instrumented range of the radar, the sweep rate

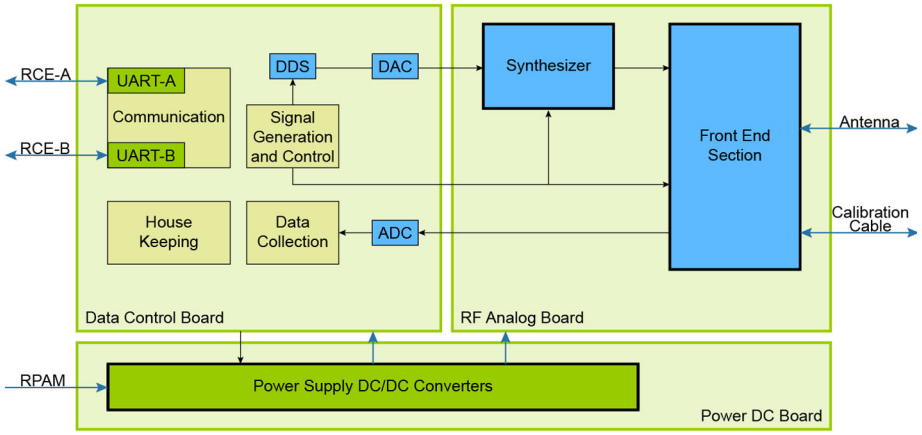

Fig. 10 Block diagram of RIMFAX electronics unit showing division into three separate boards: power-DC board, data control board and RF-analog board, all with main functions labeled

must be programmable. The sweep time for a sounding is always 100 ms. This sounding is an average of several sweeps where the sweep rate can change for each mode.

The base FMCW sweep is generated by a DDS module in the FPGA. This is converted to an analog sweep through a 14-bit DAC and a 9th order smoothing filter. The synthesizer block is controlled by the FPGA and uses frequency doublers to generate the full three-octave sweep. Signals for controlling the gating and the gain in the Front End section are generated in the signal control block.

Data collection is done with a 14-bit ADC. By oversampling the requirements to the antialiasing filter are reduced, and the dynamic range can be increased to 16 bits. This is done in a decimation filter in the FPGA.

The Front End block contains LNA, PA and gain block; devices for controlling the gain; and the switches as shown in the block diagram in Fig. 5.

Several transmission line test kits with different configurations have been made to verify the performance dictated by the mission L4 requirements:

- Kit with simulated antenna, surface reflections, and reflection at 10 m depth. The requirement is met if the deep reflection is detected with at least 10 dB Signal-to-Noise Ratio (SNR). Tests on the flight model show typically a 30 dB margin to the requirement, i.e., 40 dB measured SNR for the deep reflection.
- Kit with simulated antenna and surface reflections only. The requirement is met if the surface reflection is detected and resolved from the antenna reflection, i.e., the "valley" between the antenna and surface reflections is at least 3 dB down from the peak value at the surface reflection. Tests on the flight model show typically a 5 dB margin to the requirement.
- Kit with simulated antenna, surface reflections, and a reflection at 30 cm depth, 27 dB below the surface reflection. The requirement is met if the shallow reflection is detected and resolved from the surface reflection, i.e., the "valley" between the shallow and surface reflections is at least 3 dB down from the peak value at the shallow reflection. Tests on the flight model show typically a 5 dB margin to the requirement.

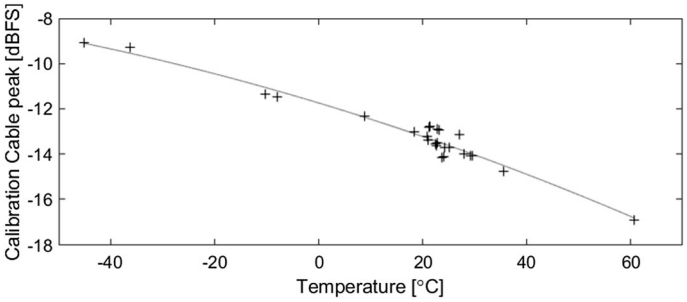

Fig. 11 Amplitude variations of calibration-cable reflections in response to temperature variations. Temperature is measured at the RF board. All measurements performed on the RIMFAX Flight Model

3.6 Calibration Cable

The RIMFAX electronics unit has two different outputs for transmitting the FMCW signal: an antenna port, where the antenna is connected via the antenna cable running through the rover bulkhead, and the calibration port, where a 2.8-m calibration cable is connected. The calibration cable is placed close to the RIMFAX electronics, inside the rover, and is shorted at the end to produce a reflection from the end of the cable. An electronic switch controls whether the calibration cable or the antenna is used.

The main purpose of the calibration cable is to provide measurements of gain variations in the transmitter and receiver. During operations on Mars the calibration cable measurements will be performed at specific distances during a traverse, for example every 10 meters, or at specific time intervals during stationary activities, for example every hour. The reflected signal from the calibration cable termination will be used to calibrate for temperature-dependent variations in radar amplitude and timing. During instrument development and qualification testing, a dependence of the calibration-cable reflection amplitude on temperature was observed (Fig. 11). There is a 7–8 dB amplitude variation when the temperature varies between −45 °C and +60 °C. Variations in time delay with temperature are negligible in the temperature range observed.

Calibration cable measurements can be used to check for short- and long-term stability and to perform temperature compensation of RIMFAX soundings through the antenna. After some time on Mars, enough data will have been collected to do trending analysis, and instrument health may be assessed when performing new calibration cable measurements.

In addition, there are at least two other calibration-cable procedures that can be explored:

1. Reduction of coherent, self-induced noise in the radar by using a passive, listening mode on the calibration port. This mode would have the same radar parameters as the mode used for soundings through the antenna.
2. Compensation for phase non-linearities in the radar sweep by using the response from the calibration cable.

3.7 Antenna

In commercial GPR systems used on Earth the antenna is normally placed on the ground or very close to the ground. This has several benefits, such as good coupling to the ground, lower radiation to the surroundings and achieving a lower frequency for a given antenna

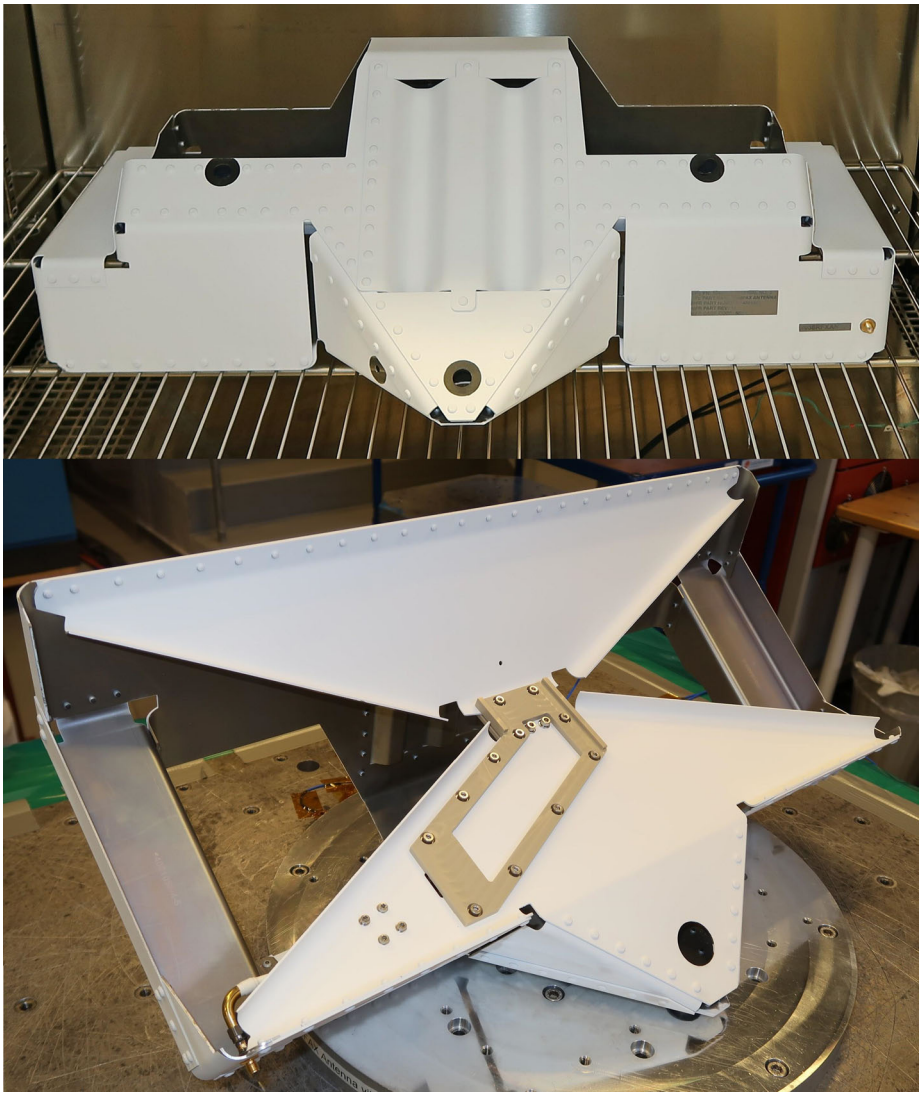

Fig. 12 The RIMFAX Flight Model SN5 antenna. Top: Front view of antenna with antenna cable connector in lower right corner. Bottom: Underside of antenna showing peak protection of central feed point, and antenna cable connector in lower left corner

size. The drawback of having the antenna on the ground is that the coupling between the antenna and ground changes as the antenna is moved.

The RIMFAX antenna (Fig. 12) is located on the rear of the Mars 2020 rover, about 60 cm above the ground (Figs. 1, 2). The antenna is an ultra-wideband bow-tie slot antenna. When designing the antenna, priority was given to having the antenna operate at as low a frequency as possible. The second priority was having as large a bandwidth as possible. The Mars 2020 project provided a particularly shaped not-to-exceed volume, which the antenna almost completely fills. Table 4 gives the major parameters characterizing the antenna.

Table 4 Parameters characterizing the RIMFAX antenna

Antenna parameter	Value
Frequency coverage	150 MHz–1200 MHz
Polarization	Linear
Return loss	<2 dB @ 150–400 MHz, <6 dB @ 400–1200 MHz
Average gain	3 dBi
Max gain	8 dBi @ 500 MHz
Size (width × length × height)	616 mm × 382 mm × 204 mm
Weight	2.21 kg

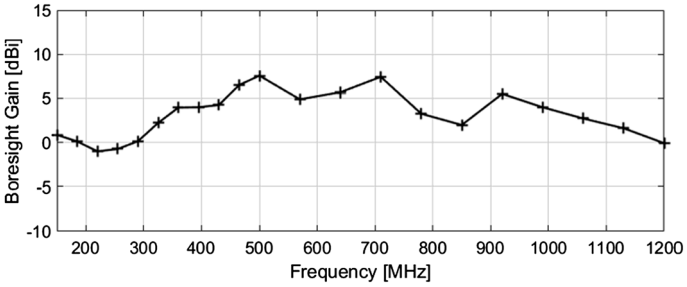

Fig. 13 Measured RIMFAX EQM antenna boresight gain at 21 frequencies between 150 MHz and 1200 MHz. Average gain is ∼3 dBi

Several antenna models were developed and tested in the field. Gain and radiation patterns of the final antenna design were characterized using the EQM in an antenna measurement range. Figure 13 shows the RIMFAX antenna gain as a function of frequency from 150 MHz to 1200 MHz. The gain varies from −1 dBi to almost 8 dBi with an average of 3 dBi. Figure 14 shows the RIMFAX antenna gain patterns in the along-drive vertical plane for discrete frequencies from 150 MHz to 1200 MHz.

Radiation patterns were measured at zero degrees, +20 degrees, and −20 degrees, at 360 degrees around the antenna. This was done in both the azimuth and elevation planes giving 6 measurement planes around the antenna. These measurements were interpolated using spherical harmonic functions to give 2D radiation patterns, shown for four frequencies in Fig. 15. While only approximations of the real antenna patterns, these patterns can give an idea of the antenna footprint size on the ground. A wide radiation pattern increases the distance over which point reflectors and dipping layers may be captured in the radargram.

The integration of the RIMFAX antenna in the Mars 2020 rover structure leads to some electromagnetic interference due to radiation coupling with the rover structure and multiple reflections between rover, ground and antenna. Figure 16 shows the 3D radiation pattern of the rover-integrated RIMFAX antenna at 200 MHz, and illustrates the coupling effects with the rover structure in combination with ground properties. The antenna pattern is computed for flat homogeneous ground with a relative permittivity of $e_r = 4$.

The strength of radiation pattern focusing within the subsurface depends on ground material properties and subsurface structure. Simulations for the RIMFAX antenna have been performed for different ground conditions. Figure 17 shows the antenna radiation pattern at 200 MHz in cross-path and along-path vertical planes for different ground properties

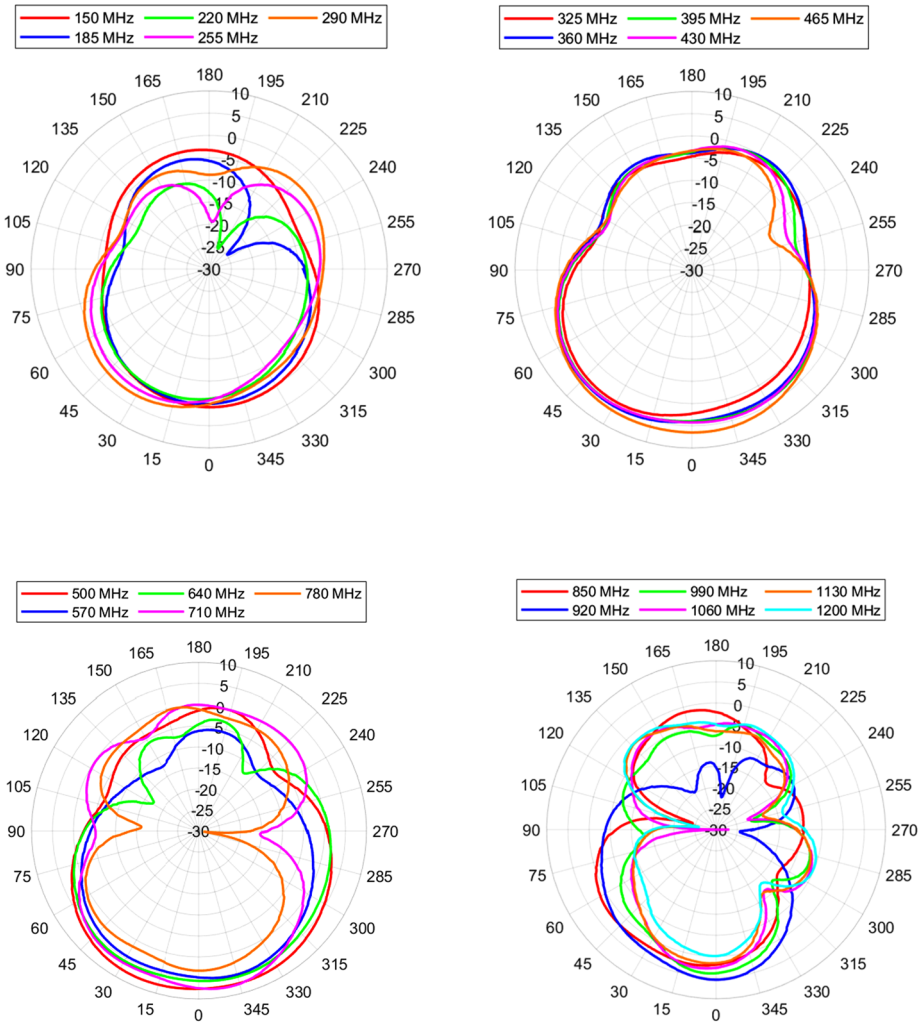

Fig. 14 Measured RIMFAX antenna gain patterns (in dBi) for 21 discrete frequencies from 150 MHz to 1200 MHz, relative to each frequency's boresight gain. Relative rover - plot orientations as follows: plane of plot is along-path vertical plane; Mars ground/surface direction is downward (0°); along-path drive direction (i.e. towards rover front) is to left (90°); antenna cross-path horizontal axis is into page (plot origin). Many lower frequencies exhibit a tilt of the downwards radiation pattern in the along-path direction of $\sim$ 5-10°

(assuming a flat surface and homogeneous, lossless subsurface conditions). The illustrated focusing effect increases with increasing relative permittivity for a homogeneous subsurface.

3.8 Modes of Operation

RIMFAX is designed to operate in different modes in which radar parameters are set to optimize data collection for different subsurface conditions. The RIMFAX gating makes it possible to omit the recording of close-range reflections, typically from the antenna and surface, which would otherwise limit the dynamic range. The removal of these reflections

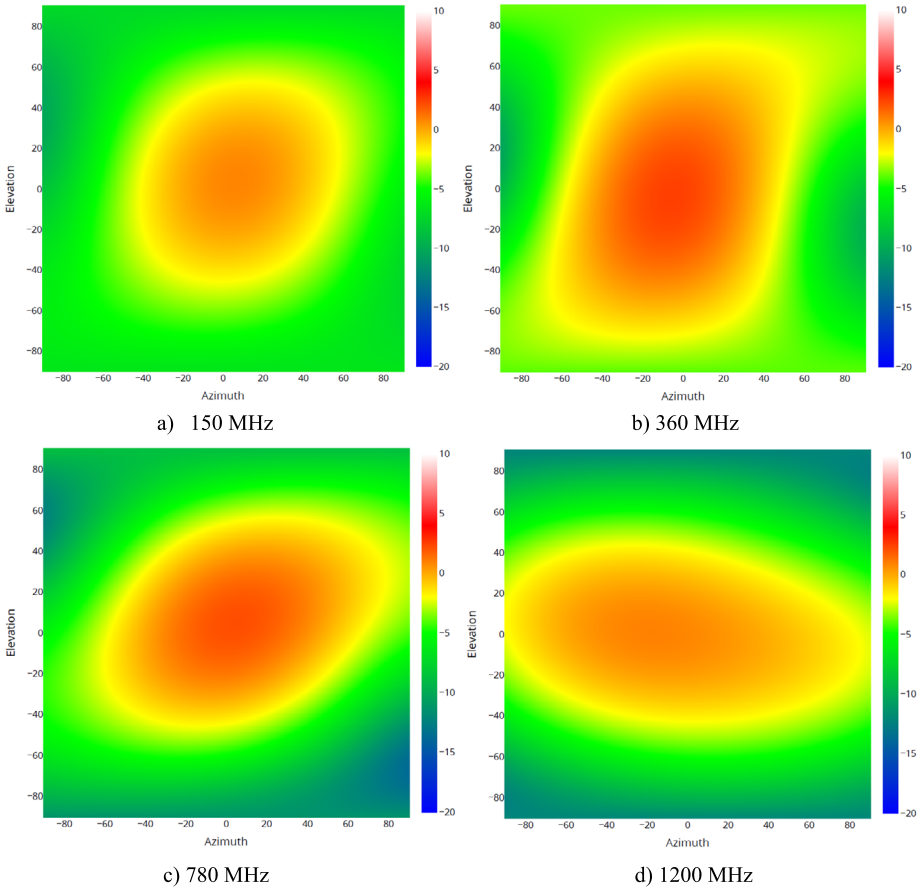

Fig. 15 Interpolated RIMFAX antenna radiation patterns (in dBi) for frequencies (**a**) 150 MHz, (**b**) 360 MHz, (**c**) 780 MHz and (**d**) 1200 MHz. Elevation is the angle measured from nadir=0° in the along-track direction; azimuth is cross track

makes it possible, when desired, to increase the radar's gain to capture weak subsurface reflections. Shifting the receiver dynamic range window particularly to each mode effectively increases the radar's total dynamic range when soundings from different modes are considered together, see Fig. 18.

The nominal plan for operation on Mars is to collect soundings from each of three modes every 5-10 cm along the rover traverse, where each mode is designed to capture data from different depths:

1. Surface Mode
   - The antenna reflection is captured in the receiver window.
   - Measures the surface reflection and the very upper subsurface only.
2. Shallow Mode
   - The antenna reflection is removed from the receiver window.
   - Measures the surface reflection and the shallow subsurface.

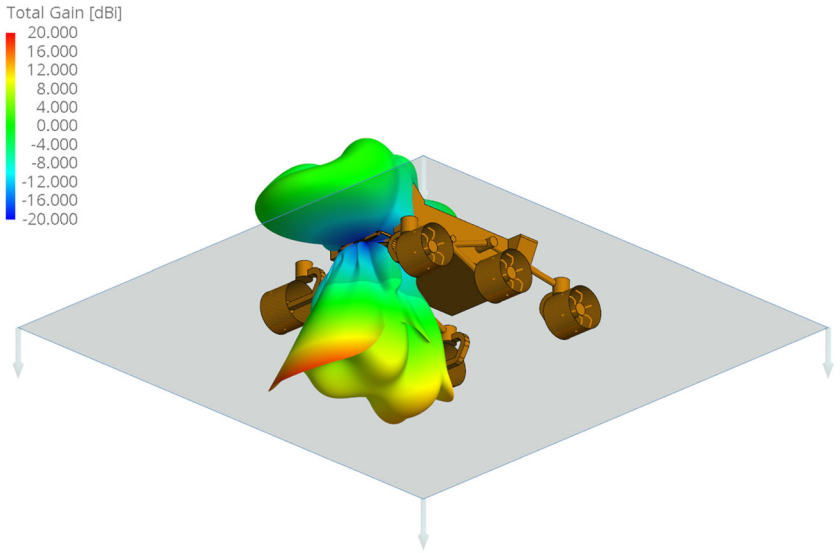

Fig. 16 3D RIMFAX antenna radiation pattern (colors) when the antenna is installed on Mars 2020 rover (Brown)

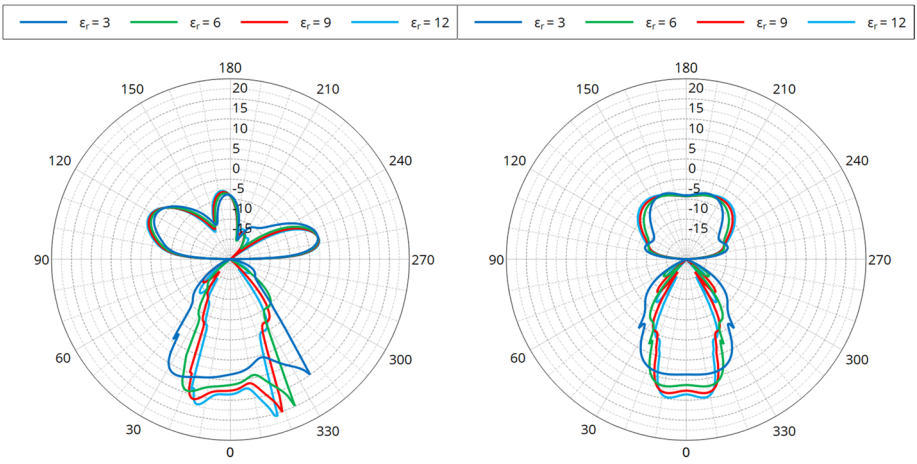

Fig. 17 RIMFAX antenna radiation patterns (in dBi) at 200 MHz, within (lower halves of curves) and above (upper halves of curves) homogeneous subsurfaces with different relative dielectric permittivities. Left: cross section of radiation pattern in along-path vertical plane (rover drive direction to left, 90°). Right: cross section of radiation pattern in cross-path vertical plane (rover drive direction into page, at plot origin)

3. Deep Mode

- The antenna and surface reflections are removed from the receiver window.
- Measures reflections from the upper subsurface (∼ 1 m depth) through the instrumented range.

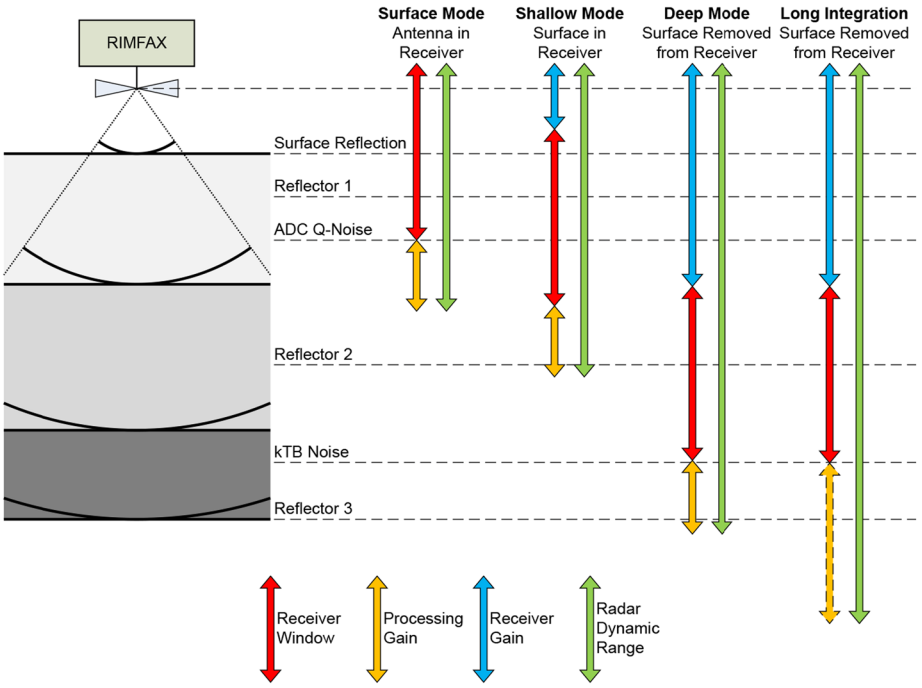

Fig. 18 Schematic representation of RIMFAX gain and dynamic range aligned to represent coverage of different subsurface zones, through the use of four operating modes. Red: RIMFAX receiver dynamic range. Yellow: increase in dynamic range from pulse compression processing. Blue: shift in dynamic range window from increase of the receiver gain. Dashed yellow: further increase of dynamics by adding together many soundings at one location (including allowance of measurement bit depth)

Table 5 RIMFAX instrumented range for a wave propagating in free space as a function of bandwidth and sweep time. Data volume per sounding given for each sweep time

		Swep time [ms]							
		100	50	25	12.5	6.25	3.125	1.5625	0.78125
Bandwidth [MHz]	450	974 m	486 m	242 m	120 m	59 m	28 m	13 m	5.4 m
	750	583 m	291 m	144 m	71 m	34 m	16 m	6.9 m	2.3 m
	1050	416 m	207 m	102 m	50 m	24 m	11 m	4.3 m	1.0 m
Data volume [bytes]		19530	9764	4882	2440	1220	610	304	152

Together, these modes extend the dynamic range of RIMFAX up to 62 dB above the dynamic range of a single mode, giving an approximate total dynamic range of 160 dB. For stationary measurements, the dynamic range can be further increased by doing a Long Integration Sounding (LIS), in which a few to several hundred soundings are summed together (on the rover RCE) to increase the processing gain.

Instrumented range and resolution can also be selected within each mode to optimize measurements based on subsurface composition and penetration depth. This is accomplished by choosing combinations of frequency range (i.e., bandwidth) and sweep time of the waveform over the frequency range, which also results in different data volumes (Table 5).

Fig. 19 General graphic representation of a notional RIMFAX drive plan, which includes a single or multiple traverse activities (2 shown here) sandwiched between Pre- and Post-Drive stationary activities

Typically, a high resolution using the full bandwidth is selected in the shallow mode, when most frequencies will be able to penetrate to the full, shallow instrumented range. In the deep mode, a narrower bandwidth limited to the lower part of the frequency range is used, and there is a tradeoff between data volume (based on number of samples per sounding) and penetration depth. Choices of sweep time are limited to the 8 values in Table 5. Bandwidth can be set between 0 and 1050 MHz (i.e., not limited to values in Table 5) within the frequency range 150-1200 MHz.

For sweep times less than 100 ms, sweeps are repeated and signal is averaged until the total collection time period reaches 100 ms. This practice ensures that the processing gain is equal for each sounding, independent of radar configuration.

In addition to nominal, active operation, RIMFAX can be operated in passive modes with the transmitter off but the receiver on, connected to either the antenna or the calibration cable. An ambient spectrum can be measured through the antenna, or an estimation of self-induced noise can be made with the calibration cable and used as an input to signal processing to increase system performance.

4 Operation on Mars

RIMFAX can acquire data either while in motion during a rover traverse or while stationary when the rover is standing still. In either state, knowledge of rover position is crucial in constructing radargrams and in correlating these radargrams with data from other instruments and with the local geology. Knowledge of time is also important to correlate RIMFAX data with other science and engineering data and to potentially extract temporal trends in the dielectric behavior of the surface and subsurface.

A set of one or more RIMFAX stationary measurements define a *Stationary Activity*, while a set of RIMFAX traverse measurements define a *Traverse Activity*. Whether planned to stand alone or as one of multiple activities executed in series, each activity is considered an individual entity in that configurations for a given activity are applicable only to that activity. Figure 19 shows a notional design for RIMFAX data gathering associated with a rover drive.

First, a Pre-Drive Stationary Activity characterizes the RIMFAX instrument and environment, both starting and concluding before the rover starts to move. A combination of one or more traverse activities can be planned for a single drive. A traverse activity will terminate in case a drive is aborted. Once a drive is terminated, the current traverse activity is stopped and a new, Post-Drive Stationary Activity, identical to the Pre-Drive one, is initiated and carried out.

4.1 Traverse Measurements and Activities

We intend to collect RIMFAX data every time the rover moves, be it for a short drive to an outcrop, a long, for a full-sol traverse, or while turning in place. It may also be the case that,

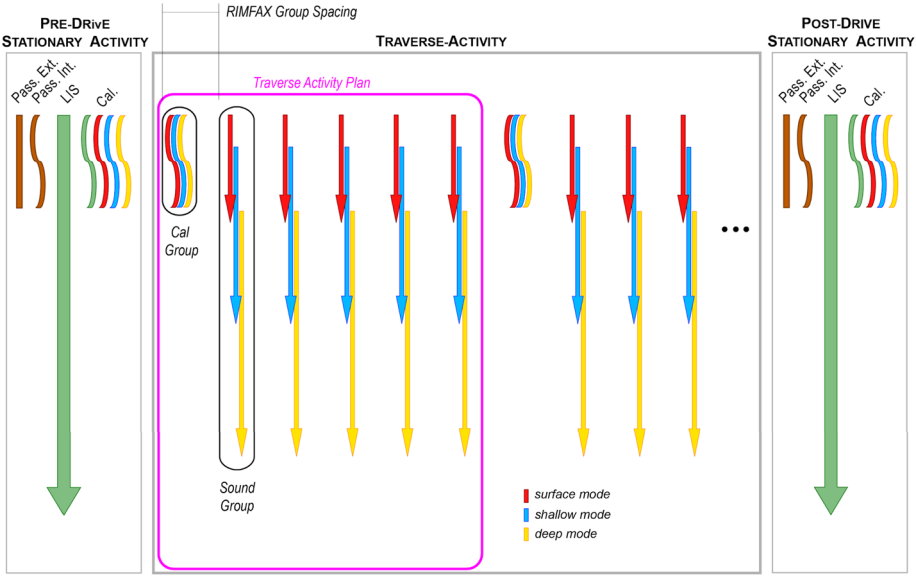

Fig. 20 Detailed graphic representation of a RIMFAX Traverse Activity, with modes being denoted by a combination of symbol, annotation and color. Modes can engage either the RIMFAX antenna or the calibration cable, and they can be passive (Receiver Only, Rx) or active (Transmitter and Receiver, Tx/Rx). Long integration soundings, or LIS, corresponds to soundings of a selected mode, repeated in rapid succession and then stacked and bit-extended on board for greater dynamic range. Pre- and Post-Drive stationary activities are identical, spaced temporally close (minutes or less) to the traverse, and commanded by time. Traverse activities have soundings organized in groups, which are commanded by distance according with a specified group spacing

when science demands, specific traverse paths will be devised to image the subsurface in three dimensions, e.g., in a "mow-the-lawn" back and forth path.

At the most basic level, all soundings collected during a traverse are organized in groups. A *sounding group* may contain one or more soundings of identical or different modes. Soundings within a group are executed in series, one immediately after the other, until the group is complete. Successive sounding groups may be identical or contain different numbers of soundings or different modes. A certain arrangement of particular sounding groups is called a *traverse activity plan*. Sounding groups are commanded according to distance and at a constant separation, configurable to values of 5 cm or larger.

Figure 20 illustrates the details of a nominal traverse activity defined by a traverse activity plan composed of 6 sounding groups. The first group consists of three active modes (surface, shallow, and deep, as explained in Sect. 3) radiated to the internal RIMFAX calibration cable. The following five groups are identical to each other and contain the same three active modes (surface, shallow, and deep) but radiated through the antenna and into the martian subsurface. This 6-group plan repeats itself until the traverse activity is complete, either at a prescribed distance or at the end of the drive.

4.2 Stationary Measurements and Activities

The collection of RIMFAX data while the rover is stationary has dual purposes. One purpose is to characterize the radiofrequency environment and the performance of the radar prior to

and after a drive, as in the stationary activities in 4.1, so that the noise floor can be measured and the traverse data properly calibrated. Another purpose is to track the radar response of the martian surface and subsurface at a single particular location over different lengths of time, up to as long as the rover is stationed there, so as to identify potential variations in dielectric properties, e.g., in response to temperature variations over the measurement time. A stationary activity is defined by a single sounding group that contains all of the desired sounding modes, which are executed sequentially and based on time alone.

4.3 Mobility and Navigation

As described in Sect. 4.1 and Fig. 20, sounding groups are executed in series. The acquisition of one sounding group must be completed before initiation of the next group, limiting the number of soundings and total time comprising one group. The amount of time necessary to collect and record each type and duration of sounding is known, and a typical group within a traverse activity plan may range (very roughly) from 300 ms to 1 s. Given typical to instantaneous expected rover speeds of 4.2 cm/s, respectively, it can be determined when a sounding group will finish execution relative to the rover's motion along the traverse toward the next distance increment (e.g., 10 cm) that will trigger the start of the next sounding subgroup. If for some reason the duration of a sounding group exceeds the span of time in which the RIMFAX antenna prescribes the selected separation distance, the subsequent group will be delayed until the previous group completes. Such a situation can arise by an excessive large group of soundings, small group separation, or excessively busy rover computer element (RCE), or a combination of these together.

The RIMFAX Instrument Manager will record a set of metadata values with each sounding that are needed to process and contextualize the sounding. Most important is the (X, Y, Z) coordinate location at which the rover perceives itself to be, within the SITE frame (Ali et al. 2005). This location is then translated to the RIMFAX antenna location, which in turn can be converted to Mars latitude, longitude and elevation coordinates. The rover's knowledge of position is calculated by the Surface Attitude Position and Pointing software module (SAPP). Position knowledge in the rover can be improved, e.g, correcting for wheel slippage with the use of visual odometry (Biesiadecki and Maimone 2006), and incorporating periodic imaging acquired bythe rover as it progresses along a drive. Further improvement in the knowledge of position can be done on the ground using partial imaging panoramas that are gridded and then localized against HiRISE orbital images (Li et al. 2011). Figure 21 shows the progression in position solution quality from the original rover-self knowledge of position, derived from its odometry visual odometry and sun sightings, to a position where visual-odometry discontinuities have been interpolated and smoothed out and HiRISE location applied to the extremities and mid-traverse points. RIMFAX has imposed a requirement for the capability of localizing soundings to within ± 50 cm in the HiRISE reference frame.

5 Field Tests and Modeling

Rimfax has been field tested at several locations, primarily in Svalbard, Norway, and in the US Southwest, between 2014 and 2019. An Engineering Model (EM) of the RIMFAX instrument has been deployed. The EM is very much like the Flight Model (FM) and differs only in some components internal to the electronics unit. The performance and functionality is the same as the FM. The antenna is an engineering model with similar performance as

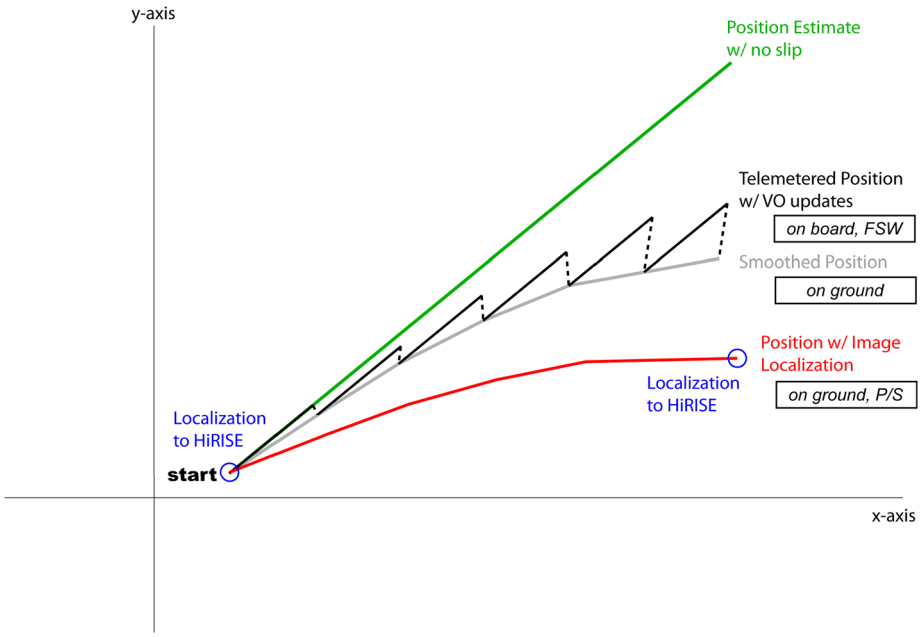

Fig. 21 Various stages of the position knowledge of the rover, which can be translated to the position of the RIMFAX antenna. Commanding of RIMFAX is done according to the onboard knowledge (green, no slip, or black, slippage with visual odometry). Localization to HiRISE requires partial or full Engineering Camera panoramas. Best position knowledge corresponds to the red path

the FM. The antenna was deployed in a flight like configuration at 60 cm above the ground during these field tests.

The purpose was several-fold: to demonstrate functionality, tune settings, and observe measurements and data gathered over various geological terrains. The last of these drivers continues to retain importance because recording what measurements of reasonably known geology here on Earth look like should help interpretations of data returned from Mars. Once on Mars, it will likely still be very useful to search out and measure specific environments on Earth that are analogous to those we suspect the Rover may have encountered during the mission. The main purpose of these tests was to verify the RIMFAX instrument performance and functionality during development of the instrument. The data collected during these campaigns have therefore not been analyzed in detail scientifically. The velocities used when converting from time to depth are typical velocities for these terrains and have not been estimated directly from the radar data collected.

5.1 Glaciers

Finding geological environments on Earth with similar electromagnetic properties to what may be expected on Mars is difficult. The subsurface of Mars is dry and cold with no free water. On Earth, free saline water may be found in the subsurface even in permafrost conditions. This makes it difficult to find places on Earth where RIMFAX can penetrate sufficiently deep (10 s of meters or more) to test its deep mode of penetration. We have therefore tested an EM-model of RIMFAX on the polythermal glacier Lovenbreen on Svalbard, Norway, where penetration is expected to be far greater than in rock(y), non-ice materials.

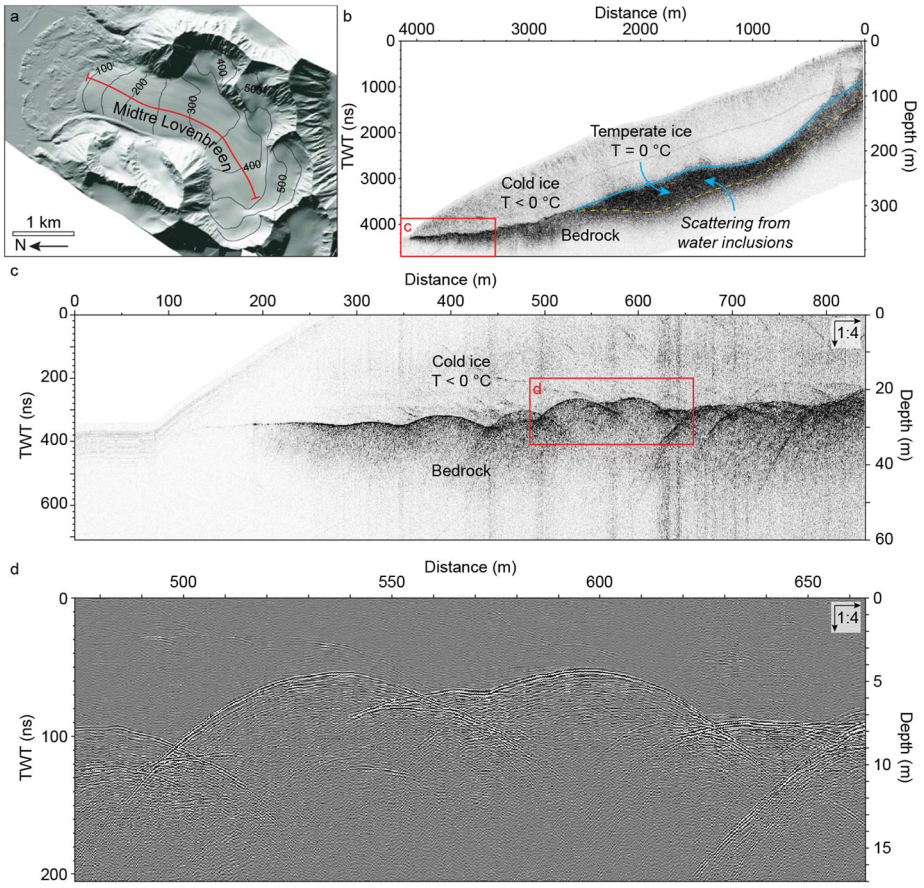

Fig. 22 RIMFAX profile from Lovenbreen glacier, Svalbard, Norway. (**a**) Regional shaded relief map with RIMFAX traverse along Lovenbreen marked in red. (**b**) Radargram (return-signal magnitude) along traverse showing cold and temperate ice zones. (**c**) and (**d**) Radargrams (return-signal magnitude and real part, respectively) enlarged from (**b**) showing clear sharp reflections along the ice/rock interface. Depth conversion uses $v = 0.167$ m/ns

Polythermal glaciers are characterized by a cold (<0 °C) surface layer several tens of meters thick overlying deeper, temperate glacial ice at or near its freezing point (Björnsson et al. 1996). This warmer ice typically contains inclusions of free water in the ice matrix. Lovenbreen glacier, ∼4 km long with an elevation span of 350 m, is cold (<0 °C) and frozen to the underlying rock over its lowermost 1.5 km, while its uppermost 1.5 km hosts a cold surface layer (<0 °C, >100 m thick) overlying temperate ice (∼0 °C).

Figure 22 shows a RIMFAX profile from the centerline of Lovenbreen. Lower and shallow zones of the glacier appear highly transparent to the GPR, while the free-water inclusions of the deep temperate ice cause heavy backscattering of radar waves. The sub-glacial ice/rock interface distinctly captured in the lower part of the glacier is obscured by this scattering in the upper, temperate part of the glacier. Because these measurements employed RIMFAX's full bandwidth (150 MHz to 1200 MHz) of frequencies that are higher than typically used on glaciers, the free-water inclusions are more pronounced in the RIMFAX data (Hagen and Sætrang 1991; Ødegård et al. 1997).

The measurements done on glaciers show that the deep RIMFAX operation modes are performing very well.

5.2 Aeolian Dunes

Aeolian sediments are abundant on Mars, including within the Mars 2020 landing site at Jezero crater. We tested the visualisation of internal structures in aeolian sediments at the Coral Pink Sand Dunes State Park, Utah. Figure 23 shows the results of a 200-m RIMFAX traverse across a transverse dune system overlying Jurassic Navajo Sandstone, as described by Ford et al. (2010). Aeolian deposits consist of three main units reaching a total thickness of $\sim$ 9 m along the profile: a basal unit made up of a 2-3 m thick sequence of parallel laminated sands; a middle unit composed of a 3-5 m sequence of climbing dune foresets; and a partially capping, uppermost unit of parallel laminated sands.

5.3 Phylloid Algae Mounds

Bioherms are moundlike reef structures built by living organisms that have diagnostic geomorphology and may have significance in the search for past life on Mars. Upper Carboniferous–Lower Permian phylloid algae (Palaeoaplysina) build-ups that occur within the Wordiekammen Formation on Svalbard are bioherms that developed on a marine carbonate platform (Hanken and Nielsen 2013). Palaeoaplysina build-ups typically have a flat-topped tabular geometry reaching $\sim$5 m thickness with diameters up to $\sim$30 m.

Here we describe the detection of these subsurface bioherms in RIMFAX field test data and demonstrate their visualisation in Fig. 24. RIMFAX profiles were taken in two primary directions: along a dipline perpendicularly crossing an outcrop of a gently dipping Palaeoaplysina-bearing horizon, and along a strikeline oriented parallel to the outcrop but set back some tens of meters in the down-dip direction. The purpose of the strikeline was to image the same Palaeoaplysina-bearing layer with the GPR at $\sim$15-20 m burial depth. An ovoid-shaped bioherm $\sim 40 \times 25$ m in plan view and up to $\sim$5 m thick was successfully detected at 5-20 m depth.

5.4 Modeling

Prior to data acquisition on Mars, computer modeling provides a first assessment of GPR imaging potential at the landing site. By understanding how measurements of subsurface layering and geological boundaries, involving complex reflections and refractions of radar waves, are manifested in a radargram, data acquisition can be designed for maximum science return. In addition, modeling can be useful as an ancillary tool for analyzing downlink data during rover operations.

Eide et al. (2019) present a modeling framework in which the spatial context is conserved through all steps, from geological mapping and construction of a subsurface model, to numerical computations and assessment of results. Using the software BGS Groundhog Desktop GSIS (Wood et al. 2015), geological interpretations from orbital imagery are used to construct subsurface models. Numerical simulations are carried out with gprMax (Warren et al. 2016) employing a finite-difference time-domain (FDTD) algorithm (Yee 1966) for simulating the propagation of radar waves in three dimensions through complex media.

Applying the modeling framework to a sample of geology in Jezero Crater, we constructed a subsurface model along a 400 meter transect, Fig. 25. The erosional scarp of Jezero's western delta is characterized by a vertical succession of transitional delta-front

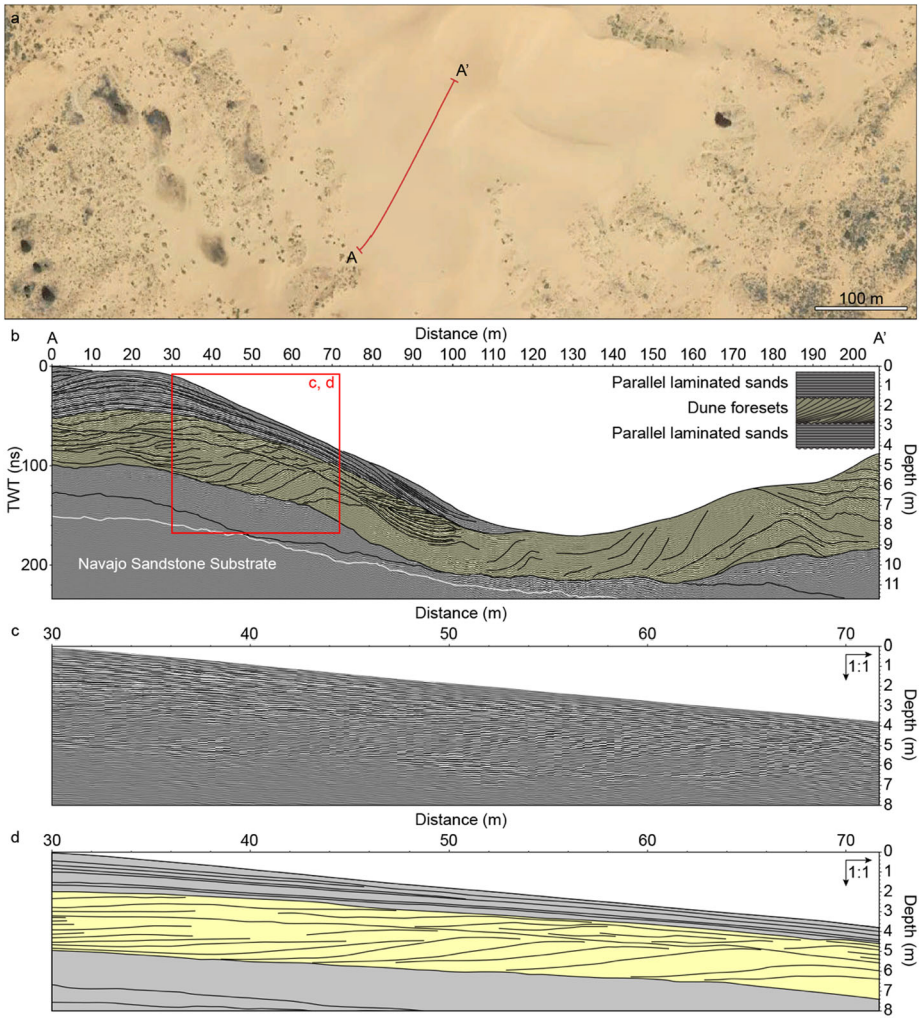

Fig. 23 RIMFAX profile from Coral Pink Sand Dunes State Park, Utah. (**a**) Google Earth satellite image with RIMFAX traverse marked in red. (**b**) Radargram along traverse with superposed sketch of internal sediment structure. A unit dominated by climbing dune foresets is sandwiched between units of parallel laminated sands. TWT denotes two-way signal travel time. (**c**) Radargram and sediment structures enlarged from (b) displayed with a horizontal-vertical scale of 1:1 (no vertical exaggeration). Yellow highlight: middle unit of dune foresets. (**d**) Radargram and sediment structures from (**a**) superposed on (**c**). Yellow highlight: middle unit of dune foresets

and prodelta deposits (Goudge et al. 2017). We interpret prodelta deposits to be present in the northern part of the transect. The prodelta unit is assigned low-loss properties with gently dipping and semi-parallel internal layering. Stratigraphically below the prodelta unit is the crater fill unit (Schon et al. 2012; Goudge et al. 2015), for which several theories of formation have been proposed (Brown et al. 2020). Here the crater fill is modeled with high scattering loss due to inhomogeneities, representing a brecciated and cemented volcanic unit. Its top surface is assigned a fractal roughness, corresponding to the rough surface expression observed in orbital imagery. This makes the uppermost crater-fill reflector distinct

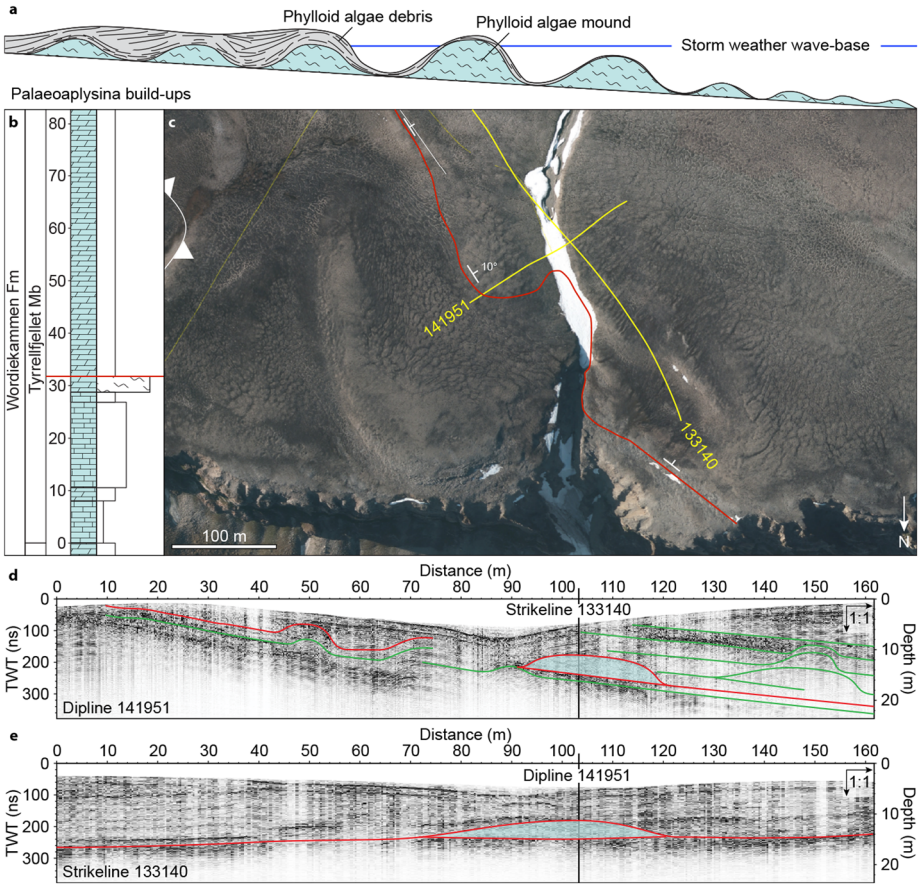

Fig. 24 RIMFAX imaging of subsurface bioherms on the Steinflaaen Plateau, Svalbard. (**a**) Cross-section illustration of Palaeoaplysina build-ups on a carbonate shelf. (**b**) Stratigraphic column showing position of Palaeoaplysina-bearing strata (capped by red line) within Wordiekammen Fm. (**c**) Steinflaaen Plateau surface composed of Wordiekammen Fm deposits. Red line: trace of surface outcrop of Palaeoaplysina-bearing strata indicated in (**b**). Yellow lines: RIMFAX transects perpendicular and parallel to strata. (**d**) and (**e**) Radargrams for dipline 141951 and strikeline 133140, respectively, showing cross section of a bioherm at location of transect intersection (vertical black line in each profile). TWT denotes two-way signal travel time. Red and green lines denote subparallel stratigraphic layering and Palaeoaplysina build-ups respectively

from internal layering in the delta units, as seen in the synthetic radargram. Where present, aeolian dunes are included as shallow features with low-loss properties. The effect of surface topography is apparent on semi-horizontal reflectors in the subsurface, especially when in combination with permittivity differences in the overburden.

6 Conclusion

RIMFAX, the ground penetrating radar instrument on the Mars 2020 Perseverance rover, will provide the science team with the capability to image the shallow subsurface. RIMFAX is an advanced frequency modulated continuous wave radar capable of operating in the 150–1200 MHz band. Its electronics are mounted inside the rover and its ultra-wide-band antenna

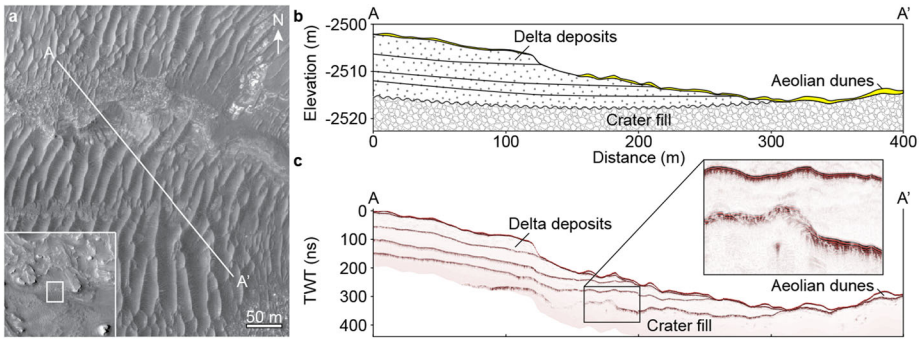

Fig. 25 Preliminary subsurface radar-wave modeling results in a sample of Jezero Crater geology. Left: location of the transect displayed on HiRISE data. Right: Schematic subsurface stratigraphy and physical model (top) and corresponding synthetic radargram resulting from numerical-simulation model (bottom)

is mounted near the back of the rover approximately 60 cm above the surface. RIMFAX will use a high-resolution sounding mode with a center frequency of 675 MHz to image the shallow subsurface, and a lower-resolution sounding mode with a center frequency of 375 MHz for deep sounding. RIMFAX will collect radar data in both sounding modes every 10 cm as the rover traverses the surface, as well as when the rover is stationary. RIMFAX prototypes have been field tested with success in glacier and permafrost conditions in Svalbard, Norway and in desert geology in Utah, USA. The depth of penetration and the depth resolution that RIMFAX will achieve on Mars will depend on the nature of subsurface materials that are encountered, which are presently unknown. Based on terrestrial field experience with radars of similar capability, RIMFAX should penetrate at least 10-meters into the Martian subsurface, which should enable it to image a range of subsurface structures which may be present, including stream channels, aeolian deposits, glacial deposits, periglacial, volcanic and impact-related features. The subsurface context provided by RIMFAX will aid the Perseverance rover in its mission to explore the ancient habitability of its field area, and select a set of promising samples for analysis, caching, and eventual return to Earth.

Acknowledgements The authors would like to thank FFI, the Norwegian Space Agency and ESA/Prodex for funding the development of the RIMFAX instrument. The authors would also like to thank Håkon Hellemo for providing the interpolated antenna diagrams. D. Nunes portion of the work was carried out at the Jet Propulsion Laboratory, California Institute of Technology, under contract with the National Aeronautics and Space Administration (80NM0018D0004).

Author Contribution Introduction: David Paige, Svein-Erik Hamran; Science Objectives: David Paige, Svein-Erik Hamran, Hans E.F. Amundsen, Lynn Carter, Henning Dypvik, Rebekka Ghent, Jack Kohler, Mike Mellon, Daniel C. Nunes, Dirk Plettemeier, Patrick Russell; Instrument development and operations: Svein-Erik Hamran, David A. Paige, Tor Berger, Sverre Brovoll, Leif Damsgård, Jo Eide, Øystein Helleren, Daniel C. Nunes, Dirk Plettemeier, Kathryn Rowe, Patrick Russell, Mats Jørgen Øyan; Field work and modelling: Svein-Erik Hamran, David A. Paige, Hans E.F. Amundsen, Tor Berger, Sverre Brovoll, Henning Dypvik, Sigurd Eide, Jack Kohler, Daniel C. Nunes, Patrick Russell, Mats Jørgen Øyan.

Funding Information Open Access funding provided by University of Oslo (incl Oslo University Hospital). This effort was carried out in part by funding from National Aeronautics and Space Administration, The Norwegian Space Agency, ESA/PRODEX, Norwegian Defence Research Establishment, Vestfonna Geophysical, and the University of Oslo.

Data availability The data are available by request.

Code availability The code used for the simulations, GPRmax, can be downloaded from https://www.gprmax.com/.

Conflict of interest Not applicable.

Publisher's Note Springer Nature remains neutral with regard to jurisdictional claims in published maps and institutional affiliations.

References

K.S. Ali, C.A. Vanelli, J.J. Biesiadecki, M.W. Maimone Yang Cheng, A.M. San Martin, J.W. Alexander, Attitude and position estimation on the Mars exploration rovers, in *2005 IEEE International Conference on Systems, Man and Cybernetics*, vol. 1 (2005), p. 20

R.E. Arvidson, J.L. Gooding, H.J. Moore, The Martian surface as imaged, sampled, and analyzed by the Viking landers. Rev. Geophys. **27**(1), 39 (1989)

N.G. Barlow, Martian Impact Craters and Their Implications for Target Characteristics (2006). https://bib.irb.hr/datoteka/951851.ESLAB40_Proceedings.pdf#page=23

J.J. Biesiadecki, M.W. Maimone, The Mars exploration rover surface mobility flight software driving ambition, in *2006 IEEE Aerospace Conference*, vol. 15 (2006)

H. Björnsson, Y. Gjessing, S.-E. Hamran, J.O. Hagen, O. LiestøL, F. Pálsson, B. Erlingsson, The thermal regime of sub-polar glaciers mapped by multi-frequency radio-echo sounding. J. Glaciol. **42**(140), 23–32 (1996)

S. Brovoll, T. Berger, Y. Paichard, O. Aardal, T.S. Lande, S.-E. Hamran, Time-lapse imaging of human heart motion with switched array UWB radar. IEEE Trans. Biomed. Circuits Syst. (2014). https://doi.org/10.1109/tbcas.2014.2359995

A.J. Brown, C.E. Viviano, T.A. Goudge, Olivine-Carbonate Mineralogy of Jezero Crater (2018). arXiv:1801.09841 [astro-ph.EP]

A.J. Brown, C.E. Viviano, T.A. Goudge, Olivine-carbonate mineralogy of the Jezero Crater region. J. Geophys. Res., Planets **125**(3) (2020). https://doi.org/10.1029/2019je006011

M.J. Campbell, J. Ulrichs, Electrical properties of rocks and their significance for lunar radar observations. J. Geophys. Res. (1969). https://doi.org/10.1029/jb074i025p05867

M.A. Chamberlain, W.V. Boynton, Response of Martian ground ice to orbit-induced climate change. J. Geophys. Res. (2007). https://doi.org/10.1029/2006je002801

V.F. Chevrier, E.G. Rivera-Valentin, Formation of recurring slope lineae by liquid brines on present-day Mars. Geophys. Res. Lett. (2012). https://doi.org/10.1029/2012gl054119

V. Ciarletti, C. Corbel, D. Plettemeier, P. Cais, S.M. Clifford, S. Hamran, WISDOM GPR designed for shallow and high-resolution sounding of the Martian subsurface. Proc. IEEE **99**(5), 824–836 (2011)

V. Ciarletti, S. Clifford, D. Plettemeier, A. Le Gall, Y. Hervé, S. Dorizon, C. Quantin-Nataf et al., The WISDOM radar: unveiling the subsurface beneath the ExoMars rover and identifying the best locations for drilling. Astrobiology **17**(6–7), 565–584 (2017)

S.M. Clifford, A model for the hydrologic and climatic behavior of water on Mars. J. Geophys. Res. **98**(E6), 10973 (1993)

S.M. Cofield, K.M. Stack, *Geologic mapping and stratigraphic analysis of a candidate Mars 2020 landing site: Jezero Crater, Mars* (2017). https://doi.org/10.1130/abs/2017AM-306001

A.B. Cunje, R.R. Ghent, A. Boivin, C-A. Tsai, D. Hickson, Dielectric properties of Martian regolith analogs and smectite clays, in *LPI Contribution*, vol. 2083 (2018), p. 1805

D.J. Daniels, *Ground Penetrating Radar*, 2nd edn. IET (2004)

C.M. Dundas, A.M. Bramson, L. Ojha, J.J. Wray, M.T. Mellon, S. Byrne, A.S. McEwen et al., Exposed subsurface ice sheets in the Martian mid-latitudes. Science **359**(6372), 199–201 (2018)

H. Dypvik, E. Kalleson, Mechanisms of late synimpact to early postimpact crater sedimentation in marine-target impact structures, in *Large Meteorite Impacts and Planetary Evolution IV* (2010). https://doi.org/10.1130/2010.2465(18)

H. Dypvik, G.S. Gohn, L.E. Edwards, J. Wright Horton Jr., D.S. Powars, R.J. Litwin, *Chesapeake Bay Impact Structure: Development of "Brim" Sedimentation in a Multilayered Marine Target* (Geol. Soc. Am., Boulder, 2018)

K.S. Edgett, R.A. Yingst, M.E. Minitti, W. Goetz, L.C. Kah, M.R. Kennedy, L.J. Lipkaman et al., Mars Hand Lens Imager (MAHLI) Efforts and Observations at the Rocknest Eolian Sand Shadow in Curiosity's Gale Crater Field Site (January 2013). https://ntrs.nasa.gov/search.jsp?R=20130009718

B.L. Ehlmann, J.F. Mustard, S.L. Murchie, J.-P. Bibring, A. Meunier, A.A. Fraeman, Y. Langevin, Subsurface water and clay mineral formation during the early history of Mars. Nature (2011). https://doi.org/10.1038/nature10582

S. Eide, S. Hamran, H. Dypvik, H.E.F. Amundsen, RIMFAX ground penetrating radar modelling: imaging the subsurface of the Jezero Western Delta, in *LPI Contribution*, vol. 2089 (2019), p. 6070

K.A. Farley, K.H. Williford, K.M. Stack, R. Bhartia, A. Chen, M. de la Torre, K. Hand, Y. Goreva, C.D.K. Herd, R. Hueso, Y. Liu, J.N. Maki, G. Martinez, R.C. Moeller, A. Nelessen, C.E. Newman, D. Nunes, A. Ponce, N. Spanovich, P.A. Willis, L.W. Beegle, J.F. Bell III, A.J. Brown, S.-E. Hamran, J.A. Hurowitz, S. Maurice, D.A. Paige, J.A. Rodriguez-Manfredi, M. Schulte, R.C. Wiens, Mars 2020 Mission Overview. Space Sci. Rev. (2020, this issue). Accepted for publication

C.I. Fassett, J.W. Head, Fluvial sedimentary deposits on Mars: ancient deltas in a crater lake in the Nili Fossae region. Geophys. Res. Lett. (2005). https://doi.org/10.1029/2005gl023456

E. Flamini, F. Fois, D. Calabrese, O. Bombaci, C. Catallo, A. Croce, R. Croci et al., Sounding Mars with SHARAD & MARSIS, in *2007 4th International Workshop on, Advanced Ground Penetrating Radar* (2007). https://doi.org/10.1109/agpr.2007.386561

R.L. Ford, S.L. Gillman, D.E. Wilkins, W.P. Clement, K. Nicoll, Geology and geomorphology of Coral Pink Sand Dunes State Park, Utah, in *Geology of Utah's Parks and Monuments, Utah Geological Association* (2010), pp. 379–406

E. Gaidos, Cryovolcanism and the recent flow of liquid water on Mars. Icarus (2001). https://doi.org/10.1006/icar.2001.6649

J.M. Goldspiel, S.W. Squyres, Groundwater discharge and gully formation on Martian slopes. Icarus (2011). https://doi.org/10.1016/j.icarus.2010.10.008

R.M. Goldstein, W.F. Gillmore, Radar observations of Mars. Science (1963). https://doi.org/10.1126/science.141.3586.1171-a

T.A. Goudge, J.F. Mustard, J.W. Head, C.I. Fassett, Constraints on the history of open-basin lakes on Mars from the composition and timing of volcanic resurfacing. J. Geophys. Res., Planets (2012). https://doi.org/10.1029/2012je004115

T.A. Goudge, J.F. Mustard, J.W. Head, C.I. Fassett, S.M. Wiseman, Assessing the mineralogy of the watershed and fan deposits of the Jezero crater paleolake system, Mars. J. Geophys. Res., Planets (2015). https://doi.org/10.1002/2014je004782

T.A. Goudge, R.E. Milliken, J.W. Head, J.F. Mustard, C.I. Fassett, Sedimentological evidence for a deltaic origin of the western fan deposit in Jezero crater, Mars and implications for future exploration. Earth Planet. Sci. Lett. (2017). https://doi.org/10.1016/j.epsl.2016.10.056

T.A. Goudge, D. Mohrig, B.T. Cardenas, C.M. Hughes, C.I. Fassett, Stratigraphy and paleohydrology of delta channel deposits, Jezero crater, Mars. Icarus (2018). https://doi.org/10.1016/j.icarus.2017.09.034

J.A. Grant, A.E. Schutz, Ground-penetrating radar as a tool for probing the shallow subsurface of Mars. J. Geophys. Res. **108**, 8024 (2003). https://agupubs.onlinelibrary.wiley.com/doi/abs/10.1029/2002JE001856@10.1002/(ISSN)2169-9100.GDMARS1

R.E. Grimm, Comparison of ground-penetrating radar and lowfrequency electromagnetic sounding for detection and characterization of groundwater on Mars, in *Sixth International Conference on Mars* (2003). https://www.lpi.usra.edu/meetings/sixthmars2003/pdf/3176.pdf

R.E. Grimm, E. Heggy, S. Clifford, Absorption and scattering in ground-penetrating radar: analysis of the Bishop Tuff. J. Geophys. Res., Planets (2006). https://doi.org/10.1029/2005JE002619

J.O. Hagen, A. Sætrang, Radio-echo soundings of sub-polar glaciers with lowfrequency radar. Polar Res. **9**(1), 99–107 (1991)

S. Hamran, Ground penetrating synthetic pulse radar: dynamic range and modes of operation. J. Appl. Geophys. (1995). https://doi.org/10.1016/0926-9851(94)00026-k

S.-E. Hamran, Radar performance of ultra wideband waveforms, in *Radar Technology* (2010). https://doi.org/10.5772/7171

S. Hamran, E. Aarholt, Glacier study using wavenumber domain synthetic aperture radar. Radio Sci. **28**(04), 559–570 (1993)

S.-E. Hamran, E. Aarholt, J. Ove Hagen, P. Mo, Estimation of relative water content in a sub-polar glacier using surface-penetration radar. J. Glaciol. **42**(142), 533–537 (1996)

S. Hamran, B. Erlingsson, Y. Gjessing, P. Mo, Estimate of the subglacier dielectric constant of an ice shelf using a ground-penetrating step-frequency radar, IEEE Trans. Geosci. Remote Sens. **36**(2), 518–525 (1998)

S.E. Hamran, V. Ciarletti, C. Corbel, D. Plettemeier, M.J. Øyan, T. Berger, L. Hanssen, The wisdom shallow sounding GPR on the ExoMars mission, in *Proc. 12th Int. Conf. Ground Penetrating Radar* (2008). http://www.eurogpr.org/joomla/images/documents/members/The%20WISDOM%20Shallow%20Sounding%20GPR%20on%20the%20ExoMars%20Mission%20by%20S.E.%20Hamran%20et%20al.pdf

N.-M. Hanken, J.K. Nielsen, Upper Carboniferous–Lower Permian Palaeoaplysina build-ups on Svalbard: the influence of climate, salinity and sea-level. Geol. Soc. (Lond.) Spec. Publ. **376**(1), 269–305 (2013)

J.C. Hanna, Hydrological modeling of the Martian crust with application to the pressurization of aquifers. J. Geophys. Res. **110**(E1), 765 (2005)

E. Heggy, S.M. Clifford, R.E. Grimm, Low-frequency radar sounding investigations of the North Amargosa Desert, Nevada: a potential analog of conductive subsurface environments on Mars. J. Geophys. Res., Planets (2006). https://doi.org/10.1029/2005JE002523

D. Hickson, A. Boivin, M.G. Daly, R. Ghent, M.C. Nolan, K. Tait, A. Cunje, C. An Tsai, Near surface bulk density estimates of NEAs from radar observations and permittivity measurements of powdered geologic material. Icarus (2018). https://doi.org/10.1016/j.icarus.2018.01.018

B.H.N. Horgan, R.B. Anderson, G. Dromart, E.S. Amador, M.S. Rice, The mineral diversity of Jezero crater: evidence for possible lacustrine carbonates on Mars. Icarus (2019). https://doi.org/10.1016/j.icarus.2019.113526

H.M. Jol, *Ground Penetrating Radar Theory and Applications* (Elsevier, Amsterdam, 2008)

E.G. Jones, Shallow transient liquid water environments on present-day Mars, and their implications for life. Acta Astronaut. (2018). https://doi.org/10.1016/j.actaastro.2018.02.027

R. Jordan, G. Picardi, J. Plaut, K. Wheeler, D. Kirchner, A. Safaeinili, W. Johnson et al., The Mars express MARSIS sounder instrument. Planet. Space Sci. (2009). https://doi.org/10.1016/j.pss.2009.09.016

S.J. Keihm, Interpretation of the lunar microwave brightness temperature spectrum: feasibility of orbital heat flow mapping. Icarus **60**(3), 568–589 (1984)

K. Lee, X. Zeng, G.A. McMechan, C.D. Howell, J.P. Bhattacharya, F. Marcy, C. Olariu, A ground-penetrating radar survey of a delta-front reservoir analog in the Wall Creek Member, Frontier Formation, Wyoming. AAPG Bull. (2005). https://doi.org/10.1306/042705040106

R. Li, S. He, Y. Chen, M. Tang, P. Tang, MER spirit rover localization: comparison of ground image– and orbital image–based methods and science applications. J. Geophys. Res., Planets (2011). https://doi.org/10.1029/2010JE003773

N. Mangold, High latitude patterned grounds on Mars: classification, distribution and climatic control. Icarus (2005). https://doi.org/10.1016/j.icarus.2004.07.030

F.J. Martín-Torres, M.-P. Zorzano, P. Valentín-Serrano, A.-M. Harri, M. Genzer, O. Kemppinen et al., Transient liquid water and water activity at Gale crater on Mars. Nat. Geosci. (2015). https://doi.org/10.1038/ngeo2412

G.M. Martínez, N.O. Renno, Water and brines on Mars: current evidence and implications for MSL. Space Sci. Rev. (2013). https://doi.org/10.1007/s11214-012-9956-3

M.T. Mellon, B.M. Jakosky, The distribution and behavior of Martian ground ice during past and present epochs. J. Geophys. Res. (1995). https://doi.org/10.1029/95je01027

M.T. Mellon, R.J. Phillips, Recent gullies on Mars and the source of liquid water. J. Geophys. Res., Planets (2001). https://doi.org/10.1029/2000je001424

M.T. Mellon, R.L. Fergason, N.E. Putzig, The thermal inertia of the surface of Mars, in *The Martian Surface* (2008). https://doi.org/10.1017/cbo9780511536076.019

H.J. Melosh, *Impact Cratering: A Geologic Process* (1989). https://ui.adsabs.harvard.edu/abs/1989icgp.book.....M/abstract

R.E. Milliken, J.F. Mustard, D.L. Goldsby, Viscous flow features on the surface of Mars: observations from high-resolution Mars Orbiter Camera (MOC) images. J. Geophys. Res., Planets **108**(E6), 5057 (2003). https://agupubs.onlinelibrary.wiley.com/doi/abs/10.1029/2002JE002005

M. Montopoli, A. Di Carlofelice, M. Cicchinelli, P. Tognolatti, F.S. Marzano, Lunar microwave brightness temperature: model interpretation and inversion of spaceborne multifrequency observations by a neural network approach. IEEE Trans. Geosci. Remote Sens. (2011). https://doi.org/10.1109/tgrs.2011.2160351

D.O. Muhleman, Microwave Emission from the Moon (January 1971). https://ntrs.nasa.gov/search.jsp?R=19720022493

D.O. Muhleman, B.J. Butler, A.W. Grossman, M.A. Slade, Radar images of Mars. Science **253**(5027), 1508–1513 (1991)

J.F. Mustard, F. Poulet, J.W. Head, N. Mangold, J.-P. Bibring, S.M. Pelkey, C.I. Fassett, Y. Langevin, G. Neukum, Mineralogy of the Nili Fossae region with OMEGA/Mars Express data: 1. Ancient impact melt in the Isidis Basin and implications for the transition from the Noachian to Hesperian. J. Geophys. Res., Planets (2007). https://doi.org/10.1029/2006je002834

J.F. Mustard, B.L. Ehlmann, S.L. Murchie, F. Poulet, N. Mangold, J.W. Head, J.-P. Bibring, L.H. Roach, Composition, morphology, and stratigraphy of Noachian crust around the Isidis Basin. J. Geophys. Res. (2009). https://doi.org/10.1029/2009je003349

J.F. Mustard, M. Adler, A. Allwood, D.S. Bass, D.W. Beaty, J.F. Bell III, W.B. Brinckerhoff, M. Carr, D.J. Des Marais, B. Drake, K.S. Edgett, J. Eigenbrode, L.T. Elkins-Tanton, J.A. Grant, S.M. Milkovich, D. Ming, C. Moore, S. Murchie, T.C. Onstott, S.W. Ruff, M.A. Sephton, A. Steele, A. Treiman, Report of the Mars 2020 Science Definition Team, 154 pp., posted July, 2013, by the Mars Exploration Program Analysis Group (MEPAG) at http://mepag.jpl.nasa.gov/reports/MEP/Mars_2020_SDT_Report_Final.pdf (2020)

R.S. Ødegård, J.O. Hagen, S.-E. Hamran, Comparison of radio–echo sounding (30–1000 MHz) and high–resolution borehole–temperature measurements at Finsterwalderbreen, Southern Spitsbergen, Svalbard. Ann. Glaciol. **24**, 262–267 (1997)

C. Olariu, J.P. Bhattacharya, X. Xu, C.L.V. Aiken, X. Zeng, G.A. McMechan, Integrated study of ancient delta-front deposits, using outcrop, ground-penetrating radar, and three-dimensional photorealistic data: Cretaceous Panther Tongue Sandstone, Utah, U.S.A. in *River Deltas-Concepts, Models, and Examples*, (2011). https://doi.org/10.2110/pec.05.83.0155

C. Ollier, C. Pain, *Regolith, Soils and Landforms* (Wiley, New York, 1996)

R. Orosei, S.E. Lauro, E. Pettinelli, A. Cicchetti, M. Coradini, B. Cosciotti, F. Di Paolo et al., Radar evidence of subglacial liquid water on Mars. Science **361**(6401), 490–493 (2018)

S. Piqueux, J. Buz, C.S. Edwards, J.L. Bandfield, A. Kleinböhl, D.M. Kass, P.O. Hayne, The MCS, Themis Teams, Widespread shallow water ice on Mars at high latitudesand midlatitudes. Geophys. Res. Lett. (2019). https://doi.org/10.1029/2019gl083947

J.J. Plaut, G. Picardi, A. Safaeinili, A.B. Ivanov, S.M. Milkovich, A. Cicchetti, W. Kofman et al., Subsurface radar sounding of the South polar layered deposits of Mars. Science **316**(5821), 92–95 (2007)

M.I. Richardson, M.A. Mischna, Long-term evolution of transient liquid water on Mars. J. Geophys. Res., Planets (2005). https://doi.org/10.1029/2004je002367

C. Sætre, H. Hellevang, L. Riu, H. Dypvik, C. Pilorget, F. Poulet, S.C. Werner, Experimental hydrothermal alteration of basaltic glass with relevance to Mars. Meteorit. Planet. Sci. (2019). https://doi.org/10.1111/maps.13214

S.C. Schon, J.W. Head, C.I. Fassett, An overfilled lacustrine system and progradational delta in Jezero crater, Mars: implications for Noachian climate. Planet. Space Sci. (2012). https://doi.org/10.1016/j.pss.2012.02.003

R.A. Schultz, H.V. Frey, A new survey of multiring impact basins on Mars. J. Geophys. Res. (1990). https://doi.org/10.1029/jb095ib09p14175

S. Shahrzad, K.M. Kinch, T.A. Goudge, C.I. Fassett, D.H. Needham, C. Quantin-Nataf, C.P. Knudsen, Crater statistics on the dark-toned, mafic floor unit in Jezero crater, Mars. Geophys. Res. Lett. (2019). https://doi.org/10.1029/2018gl081402

A. Shaw, R.E. Arvidson, R. Bonitz, J. Carsten, H.U. Keller, M.T. Lemmon, M.T. Mellon, M. Robinson, A. Trebi-Ollennu, Phoenix soil physical properties investigation. J. Geophys. Res., Planets **114**(E1), E00E05 (2009). https://doi.org/10.1029/2009JE003455

S.W. Squyres, M.H. Carr, Geomorphic evidence for the distribution of ground ice on Mars. Science **231**(4735), 249–252 (1986)

D. Stillman, G. Olhoeft, Frequency and temperature dependence in electromagnetic properties of Martian analog minerals. J. Geophys. Res. (2008). https://doi.org/10.1029/2007je002977

R. Sullivan, R. Anderson, J. Biesiadecki, T. Bond, H. Stewart, Cohesions, friction angles, and other physical properties of Martian regolith from Mars exploration rover wheel trenches and wheel scuffs. J. Geophys. Res., Planets **116**(E2), E02006 (2011). https://doi.org/10.1029/2010JE003625

F.T. Ulaby, T.H. Bengal, M.C. Dobson, J.R. East, J.B. Garvin, D.L. Evans, Microwave dielectric properties of dry rocks. IEEE Trans. Geosci. Remote Sens. (1990). https://doi.org/10.1109/36.54359

C. Warren, A. Giannopoulos, I. Giannakis, gprMax: open source software to simulate electromagnetic wave propagation for ground penetrating radar. Comput. Phys. Commun. (2016). https://doi.org/10.1016/j.cpc.2016.08.020

T.R. Watters, B. Campbell, L. Carter, C.J. Leuschen, J.J. Plaut, G. Picardi, R. Orosei et al., Radar sounding of the medusae fossae formation Mars: equatorial ice or dry, low-density deposits? Science **318**(5853), 1125–1128 (2007)

S.C. Werner, The Early Martian evolution—constraints from basin formation ages. Icarus (2008). https://doi.org/10.1016/j.icarus.2007.12.008

B. Wood, T. Richmond, J. Richardson, J. Howcroft, *BGS Groundhog® Desktop Geoscientific Information System External User Manual* (British Geological Survey, Nottingham, 2015). http://nora.nerc.ac.uk/id/eprint/511792/

K. Yee, Numerical solution of initial boundary value problems involving Maxwell's equations in isotropic media. IEEE Trans. Antennas Propag. (1966). https://doi.org/10.1109/tap.1966.1138693